Bulletin of Volcanology (2024) 86:69
https://doi.org/10.1007/s00445-024-01761-5

RESEARCH ARTICLE

Generation of deposit-derived pyroclastic density currents by repeated crater rim failures at Stromboli Volcano (Italy)

Federico Di Traglia[1,2] · Paolo Berardino[2] · Lorenzo Borselli[3,4] · Pierfrancesco Calabria[1] · Sonia Calvari[5] · Daniele Casalbore[6,7] · Nicola Casagli[8,9] · Francesco Casu[2] · Francesco Latino Chiocci[6,7] · Riccardo Civico[10] · Walter De Cesare[1] · Claudio De Luca[2] · Matteo Del Soldato[8] · Antonietta Esposito[1] · Carmen Esposito[2] · Massimiliano Favalli[11] · Alessandro Fornaciai[11] · Flora Giudicepietro[1,2] · Teresa Gracchi[8,9] · Riccardo Lanari[2] · Giovanni Macedonio[1,2] · Fernando Monterroso[2] · Antonio Natale[2] · Teresa Nolesini[12] · Stefano Perna[2,13] · Tullio Ricci[10] · Claudia Romagnoli[7,14] · Guglielmo Rossi[12] · Carlo Tacconi Stefanelli[8]

Received: 7 April 2024 / Accepted: 30 June 2024 / Published online: 8 July 2024

Abstract

The gravitational instability of hot material deposited during eruptive activity can lead to the formation of glowing avalanches, commonly known as deposit-derived pyroclastic density currents (PDCs). These currents can travel hundreds of metres to several kilometres from the source at exceptionally high temperatures, posing a catastrophic hazard to areas surrounding steep-slope volcanoes. The occurrence of deposit-derived PDCs is often associated with crater rim failure, which can be triggered by various factors such as magma thrust from dike injection, magma fingering, bulging or less commonly, powerful explosions. Here, the in-depth study of data from the multi-parametric monitoring network operating on Stromboli (Italy), including video surveillance, seismicity and ground deformation data, complemented by remote topographic sensing data, has facilitated the understanding of the events leading to the crater rim collapse on 9 October and 4 December 2022. The failures resulted in the remobilisation of $6.4 \pm 1.0 \times 10^3$ m^3 and $88.9 \pm 26.7 \times 10^3$ m^3 of material for the 9 October and the 4 December 2022, respectively, which propagated as PDCs along the NW side of the volcano and reached the sea in a few tens of seconds. These events were characterised by a preparatory phase marked by an increase in magmatic pressure in the preceding weeks, which correlated with an increase in the displacement rate of the volcano's summit. There was also an escalation in explosive degassing, evidenced by spattering accompanied by seismic tremors in the hours before the collapse. These events have been interpreted as an initial increase in magma vesicularity, followed by the release of gas once percolation threshold was reached. The degassing process induced densification of the magma, resulting in increased thrust on the conduit walls due to increased magmastatic pressure. This phase coincided with crater rim collapse, often followed or accompanied by the onset of lava overflow phases. A mechanism similar to the one proposed may shed light on similar phenomena observed at other volcanoes. The analysis performed in this study highlights the need for a multi-parametric and multi-platform approach to fully understand such complex phenomena. By integrating different data sources, including seismic, deformation and remote sensing data, it is possible to identify the phenomena associated with the different phases leading to crater rim collapse and the subsequent development of deposit-derived PDCs.

Keywords Deposit-derived PDC · Crater rim collapse · Volcano monitoring · Topographic change detection · Stromboli · Aeolian archipelago

Riassunto

L'instabilità del materiale vulcanoclastico caldo depositato durante l'attività eruttiva può condurre alla formazione di correnti piroclastiche, dette anche valanghe ardenti. Questi flussi possono spostarsi da distanze che vanno da centinaia di metri a diversi chilometri dalla sorgente, mantenendo temperature estremamente elevate, rappresentando così un rischio significativo

Editorial responsibility: V. Acocella

Extended author information available on the last page of the article

per le aree circostanti i vulcani caratterizzati da pendii ripidi. La manifestazione di tali fenomeni è frequentemente associata al collasso del bordo del cratere, evento che può essere innescato da vari fattori quali la pressione esercitata dal magma, l'intrusione di dicchi, il rigonfiamento o, meno frequentemente, intense esplosioni. Nel presente studio, l'analisi dettagliata dei dati provenienti dalla rete di monitoraggio multiparametrico installata a Stromboli (Italia), che include informazioni riguardanti sorveglianza video, sismicità e deformazioni del suolo, integrate da dati topografici ottenuti tramite telerilevamento, ha facilitato l'identificazione dei fattori che hanno portato ai crolli del bordo del cratere avvenuti il 9 ottobre e il 4 dicembre 2022. Tali collassi hanno comportato la rimobilizzazione rispettivamente di $6.4 \pm 1.0 \times 10^3$ m^3 e $88.9 \pm 26.7 \times 10^3$ m^3 di materiale, il quale si è propagato sotto forma di correnti piroclastiche lungo il versante nord-occidentale del vulcano, raggiungendo il mare in poche decine di secondi. Questi eventi sono stati caratterizzati da una fase preparatoria caratterizzata da un aumento della pressione magmatica nelle settimane precedenti, correlato ad un incremento del tasso di deformazione. Inoltre, nelle ore precedenti il collasso, si è registrata una intensificazione del degassamento esplosivo, evidenziata da frequenti esplosioni di piccola entità accompagnate da un incremento del tremore sismico. Tali eventi sono stati interpretati come un iniziale aumento della vescicolarità del magma, seguito dal rilascio di gas. Il processo di degassamento ha quindi portato ad un addensamento del magma, con conseguente aumento della pressione sulle pareti del condotto magmatico. Questa fase ha coinciso con il crollo del bordo craterico, seguito o accompagnato da fasi di tracimazione lavica. Un meccanismo simile a quello proposto potrebbe fornire indicazioni utili per la comprensione di fenomeni analoghi osservati in altri vulcani. L'analisi condotta in questo studio sottolinea l'importanza di un approccio multiparametrico e a piattaforma multipla per una migliore comprensione di fenomeni così complessi. Integrando diverse tipologie di dati, tra cui informazioni sismiche, di deformazione del suolo e di telerilevamento, è possibile identificare i fenomeni associati alle diverse fasi che portano al collasso del bordo del cratere e al conseguente sviluppo di correnti piroclastiche.

Introduction

The gravitational instability of material deposited during eruptive activity, whether it is due to the collapse of crater rims or the failure of hot deposits on the flanks of volcanic cones, typically results in the formation of glowing avalanches. These extremely hazardous, small-volume (10^3–10^7 m^3), deposit-derived pyroclastic density currents (PDCs) can suddenly remobilise previously deposited tephra (Alvarado et al. 2023) and travel at extremely high temperatures from hundreds of metres to several kilometres from the source area (Lube et al. 2007; Lerner et al. 2022). Deposit-derived PDCs are significantly more common than originally thought, as evidenced by the increase in observations in recent decades, and are relatively common in mafic-intermediate volcanoes characterised by steep slope gradients. Incandescent avalanches have been documented at several sites, including the 1974 eruption of Fuego volcano in Guatemala (Davies et al. 1978) and the 1975 eruption of Ngauruhoe volcano in New Zealand (Nairn and Self 1978). At Ngauruhoe volcano, deposit-derived PDCs were reported to have formed from the remobilisation of proximal, poorly welded volcaniclastic agglutinate (Lube et al. 2007), as also observed during the 1822 and 1944 eruption of Mt. Vesuvius (Monticelli and Covelli 1823; Hazlett et al. 1991; Arrighi et al. 2001; Cagnoli et al. 2015) and the 2002 eruption of Stromboli (Pioli et al. 2008). Evidence of deposit-derived PDCs has been found on the flanks of volcanoes such as Arenal and Rincon de la Vieja in Costa Rica (Alvarado and Soto 2002; Cole et al. 2005; Baez et al. 2024), Tungurahua in Ecuador (Kelfun et al. 2009; Bernard et al. 2014, 2016), Mt. Etna in Italy (Calvari and Pinkerton 2002; Behnke et al. 2008; Martino et al. 2015a,b; Andronico et al. 2018) and Mt. Fuji in Japan (Yamamoto et al. 2005). On 3 June 2018, a deposit-derived PDC sequence occurred once more at Fuego volcano, and it tragically resulted in an estimated death toll of > 400 fatalities (Albino et al. 2020; Risica et al. 2022; Charbonnier et al. 2023) and up to 2900 due to unregistered people believed to be missing (Naismith et al. 2020). In general, two types of deposit-derived PDCs can be defined: (i) those triggered by magma thrust (dike injection, magma fingering or bulging) or, more rarely, powerful explosions (Cole et al. 2005; Calvari et al. 2016; Di Traglia et al. 2018a, 2023a) and (ii) those generated by the failure of hot material deposited on volcanic flanks (Di Roberto et al. 2014; Bernard et al. 2014; Salvatici et al. 2016; Giordano and De Astis 2021). In the latter case, loose volcaniclastic material may collapse simply by exceeding the angle of friction, or by additional mechanisms such as undercutting or overloading of the slope by PDCs or lava flows. Deposit-derived PDCs are potentially hazardous to communities living near volcanoes and to tourists. To improve the hazard assessment associated with these phenomena, it is necessary to enlarge the understanding of hot rock failure, considering the role and effect of different predisposing factors (i.e. lithological features; topographic variations) and triggers (i.e. slope overloading, magma thrust, seismicity, etc.). All these aspects, if well understood, can be effectively monitored using advanced analytical techniques and appropriate numerical modelling, to anticipate hot rock failure and the development of glowing avalanches. To this end, an in-depth analysis of the occurrence of deposit-derived PDCs at Stromboli, Italy,

during the period October–December 2022 has been undertaken. The analysis includes direct volcanological observations, geophysical monitoring data, topographic surveys and slope stability modelling. The primary objective of this study is to identify the factors that have contributed to the predisposition and the mechanisms responsible for the collapse of the deposits and the generation of PDCs. Stromboli represents an ideal case to study these phenomena due to their frequent recurrence (Calvari and Nunnari 2023; Di Traglia et al. 2023a) and the large amount of volcanological, geophysical and geomorphological monitoring data available for each episode. Our results will help to assess the hazard and to mitigate the risk posed by deposit-derived PDCs in the short and long term, by contributing to the interpretation of monitoring data from active volcanoes, to integrated hazard assessment and to their proper territorial planning.

Stromboli volcano and its recent activity.

Stromboli is a volcanic island in the Aeolian archipelago in the southern Tyrrhenian Sea (Fig. 1a–b). The volcano has undergone different phases of activity, often accompanied by flank instability events on its NW and SE slopes (Romagnoli et al. 2009a and 2009b). The NW flank of the volcano, locally referred to as "Sciara del Fuoco" (SdF, Fig. 1c–d), took shape after a series of lateral collapses, the most recent of which occurred around the sixth millennium BP (Speranza et al. 2008). This collapse event resulted

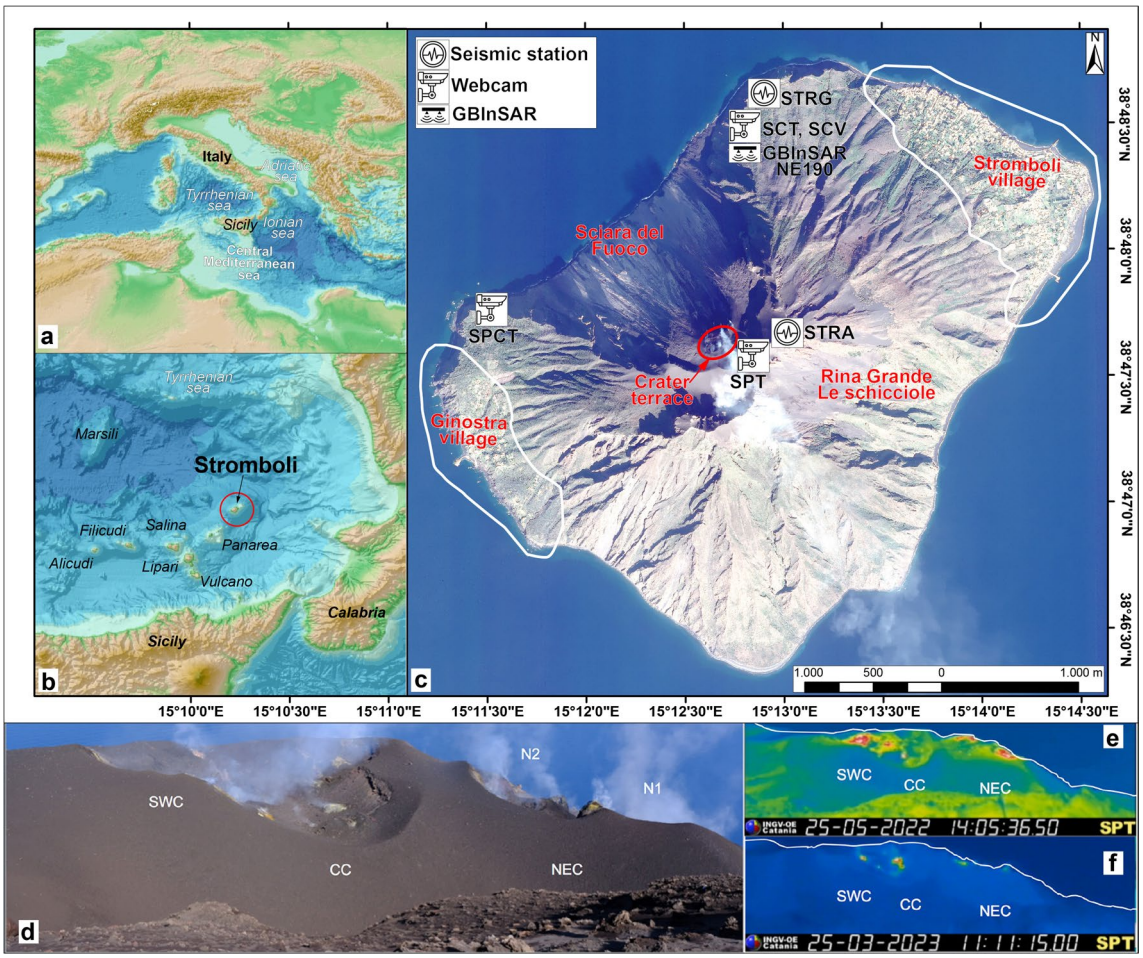

Fig. 1 Geographical context of Stromboli volcano within **a** the central Mediterranean and **b** the southern Tyrrhenian Sea. **c** Orthophoto obtained from the PLEIADES-1 acquisition on 11 February 2023, showing the island of Stromboli and delineating the positions of the villages of Stromboli and Ginostra, as well as the two unstable flanks of the volcano: NW—Sciara del Fuoco and SE—Rina Grande-Le Schicciole areas. The location of the monitoring stations used in this study also included SCV (visible webcam), SCT, SPT, SPCT (thermal webcams), GBInSAR NE190 (interferometric radar), STRA and STRG (seismic stations). The active craters are located in the upper part of the Sciara del Fuoco, indicated by the red ellipse. **d** Photo of the summit craters (courtesy of F. Ciancitto) from the south on 12 June 2023. The field of view is ~ 300 m wide. SWC, SW crater zone; CC, central crater zone; NEC, NE crater zone, including the two vents N1 and N2. **e** Thermal image taken by the SPT camera on 25 May 2022 at 14:05:36 UTC showing the three crater zones SWC, CC and NEC. The white line indicates the crater outline. **f** Thermal image taken by the SPT camera on 25 March 2023 at 11:11:15 UTC showing the three crater zones SWC, CC and NEC. The white line shows the crater outline and highlights the changes that have occurred since May 2022. The view of **e** and **f** is similar to the image in d

in a repositioning of the eruptive activity within the collapsed area. The volcano has three crater areas—WC, CC and NEC—and a variable number of active vents (N1 and N2; Fig. 1e–g) as a function of the magma level within the conduit (Spampinato et al. 2008) and the resulting intensity of eruptive activity.

The steep topography and frequent eruptive activity result in the irregular deposition of heterogeneous layers of volcaniclastic materials (both fine- and coarse-grained) and lava of varying thickness (Kokelaar and Romagnoli 1995; Casalbore et al. 2010, 2011; Di Traglia et al. 2018b), that make both the SdF area and the crater zone (Fig. 1c) at its upper boundary susceptible to instability events of diverse magnitude (Apuani et al. 2005; Di Traglia et al. 2018c, 2018d). These events range from persistent, small-scale rockfalls and debris slides to volcanic slope deformations, occasionally culminating in rock or debris avalanches (Tibaldi 2001; Apuani et al. 2005; Chiocci et al. 2008; Tibaldi et al. 2009; Casalbore et al. 2020; Di Traglia et al. 2023b), which can cause tsunamis that can affect both the coasts of Stromboli and the surrounding islands and regions (Rosi et al. 2019; Pistolesi et al. 2020; Turchi et al. 2022).

The style of eruptive activity characteristic of Stromboli is referred to as "Strombolian" and was first described by Mercalli in 1883 as "slightly explosive eruptions occurring at discrete but relatively regular intervals of seconds or minutes". Over time, various classifications of Strombolian activity have been proposed to distinguish both the differences in the so-called "ordinary" or persistent activity, which involves the ejection of materials with varying grain-size and gas/fragment content to heights that typically do not exceed 100–200 m above the craters (Patrick et al. 2007; Giudicepietro et al. 2022), and more intense explosive events, categorised as "major explosions" or "paroxysms" (also referred as "Basaltic Vulcanian" by Giordano and De Astis 2021) on the basis of the magnitude of the explosions (Barberi et al. 1993; Rosi et al. 2013; Bevilacqua et al. 2020; Calvari et al. 2021; Voloschina et al. 2023). In addition to explosive activity, Stromboli frequently produces effusive activity, including both small and short-lived lava flows of tens of metres in length spreading within the crater terrace, or lava overflows extending over the crater rim for tens to hundreds of metres and lava effusions from lateral vents or central craters, some of which can last for several months, with lava emissions on the order of 10^6 to 10^7 m^3 (e.g. Marsella et al. 2012; Bosman et al. 2014; Di Traglia et al. 2020, 2022; Civico et al. 2021; Casalbore et al. 2022; Calvari and Nunnari 2023). On Stromboli, the occurrence of deposit-derived PDCs is common and primarily originates from the collapse of the NE crater rim (Fig. 1e), although it should be noted that similar phenomena can occur after paroxysmal events/Vulcanian explosions when the spatter accumulation fails, as happened in 1930, 1944 and 2019 (Di Roberto et al. 2014; Giordano and De Astis 2021). Crater rim failures are typically initiated by effusive phenomena, with overflows being the most frequent triggers, and less commonly, flank eruptions (Calvari and Nunnari 2023; Di Traglia et al. 2023a, b). It is even less common for crater rim collapses to be associated with intense explosive events, although such instances have been observed, as was the case on 16 November 2020 (Calvari et al. 2021; Vossen et al 2022). During the period investigated in this work, spanning between May 2022 and March 2023, the persistent Strombolian explosive activity at the crater terrace was accompanied by some major explosions and overflows from the craters, as summarised in Table 1.

Materials and methods

The continuous monitoring of Stromboli's eruptive activity and the quantification of the explosive activity recorded at the summit vents have been carried out by manual analysis of the images recorded by the fixed monitoring camera network operated by the INGV-OE (Istituto Nazionale di Geofisica e Vulcanologia-Osservatorio Etneo). These are three thermal cameras located at Il Pizzo Sopra La Fossa (SPT), Punta dei Corvi (SPCT) and Semaforo Labronzo (SCT), and one visible camera located at Semaforo Labronzo (SCV). The position of the cameras is displayed in Fig. 1d. The explosion count was carried out mainly on the images recorded by the SCT camera while, between 14:28 and 17:30 on 4 December 2022, when the PDCs were obscuring the sight from this position, the explosion count was carried out from SPT. The list of INGV surveillance cameras in operation on Stromboli during 2022 and their main characteristics are reported in the Online Resources.

Seismic network and seismological analysis

The Stromboli permanent seismic network consists of eight stations equipped with broadband sensors to study seismic source processes associated with volcanic activity. The seismic stations, strategically positioned for azimuthal coverage, are spaced at distances ranging from about 350 to 1200 m. Power is provided in remote locations by battery and solar panel systems. Most of the seismic stations use Guralp CMG40T broadband velocimeters, and recent new stations include 3ESPC broadband velocimeters at selected locations. Data is digitally recorded and transmitted in real-time to the INGV monitoring centres of Osservatorio Vesuviano and Osservatorio Etneo. The network has continuously monitored Stromboli, serving scientific research and tourism and contributing to public safety since its installation in 2003 (De Cesare et al. 2009).

Table 1 List of the eruptive events occurred at Stromboli volcano during the time span here considered. *NEC*, NE crater; *CC*, central crater; *SWC*, SW crater; *PDC*, pyroclastic density current. Times are reported in UTC. *SCT*, thermal camera located at Labronzo, ~ 100 m a.s.l. on the north flank of the volcano. *SCV*, visible camera located at Labronzo, same position as SCT. *SPCT*, thermal camera located at Punta dei Corvi, western flank of Stromboli volcano, at ~ 100 m a.s.l. *SPT*, thermal camera located at Il Pizzo Sopra La Fossa, 850 m a.s.l. See Fig. 1 for camera locations. Data from Calvari and Nunnari (2023) and Giodicepietro et al. (2023). For more details, monitoring reports can be found at https://cme.ingv.it/bollettini-e-comunicati

Date (dd/mm/yyyy)	Time (UTM)	Eruptive activity	Duration	Monitoring camera label
03/10/2022	09:08– > 16:00	Lava overflow from NEC	7 h	SCT, SCV, SPCT
03/10/2022	09:40	Small failure of NE crater	1 h	SCT, SCV, SPCT
04/10/2022	09:07– > 12:00	Lava overflow from NEC	3 h	SCT, SCV, SPCT
07/10/2022	22:15	Lava overflow from NEC	3 h	SCT, SCV, SPCT
09/10/2022	07:22	Lava overflow from NEC	5 days	SCT, SCV, SPCT
09/10/2022	07:22	NE crater failure + PDCs		SCT, SCV, SPCT
09/10/2022	07:43	Several PDC from overflow front crumbling. Canyon formation	9–10 days	SCT, SCV, SPCT
16/11/2022	14:28	Small failure of NE crater		SPT, SCT, SCV, SPCT
04/12/2022	12:08– > 17:30	Lava overflow from NEC	~ 5 h	SCT, SCV, SPCT, SPT
04/12/2022	12:08	NE crater failure + PDCs		SCT, SCV, SPCT, SPT
05/12/2022	08:40– > 17:00	Lava overflow from NEC	9.5 h	SCT, SCV, SPCT, SPT
06/12/2022	14:48– > 21:00	Lava overflow from NEC	~ 8 h	SCT, SCV, SPT
07/12/2022	00:00– >	Intracrater flow + overflow	2.5 days	SCT, SCV, SPT
16/12/2022	9:50– > 16:30	Lava overflow from NEC	6.5 h	SPT, SCT, SCV, SPCT
19/12/2022	14:00– > 16:00	Lava overflow from NEC	2 h	SPCT
21/12/2022	09:08	Major explosion from SWC		SCT, SCV, SPCT
26/12/2022	17:17	Major explosion from SWC + CC		SCT, SCV, SPCT
27/12/2022	05:53 + 20:49	2 Lava overflows	~ 24 h	SCT, SCV, SPCT

We examined data from a seismic station located close to the craters, specifically STRA, which is about 500 m from the N2 vent (Fig. 1c). In our analysis, the time series of seismic amplitude, referred to as RSAM (real-time seismic amplitude measurement) (Endo and Murray 1991), were computed over different frequency ranges and with an accuracy of 1-min time window. In particular, we focused on the 1–7 Hz frequency band, characteristic of the seismic precursors of overflows identified by Giudicepietro et al. (2023), and the > 10 Hz frequency range, indicative of landslides and block movement from the front of lava flows on the Sciara del Fuoco, as argued in previous work by Giudicepietro et al. (2023). We used the ObsPy system (Beyreuther et al. 2010; Megies et al. 2011; Krischer et al. 2015) to filter the signal and produce seismogram and spectrogram plots. We analysed the events of 9 October and 4 December 2022, extending the analysis over a 6-day period, specifically from 8 to 13 October and from 3 to 8 December 2022. The aim was to identify possible seismic signals generated by processes affecting the volcano's crater rim, such as landslides and PDCs.

Ground deformation measurements

Ground displacements on Stromboli have been monitored using a ground-based synthetic aperture radar working in interferometric mode (GBInSAR) system installed at the northern edge of the SdF at an elevation of 190 m above sea level (a.s.l.; GBInSAR NE190 in Fig. 1d). This system observes the central and northern areas of the crater terrace and the corresponding sections of the SdF, except for shaded areas (due to irregular morphology) or altitudes below 200 m a.s.l. (Di Traglia et al. 2021). GBInSAR systems are remote sensing imaging devices that transmit and receive microwave pulses while moving physical antennas along a track (Di Traglia et al. 2021 and references therein). These systems are designed to measure one-dimensional ground motion along the line of sight (LOS) of the sensor by exploiting the phase difference between acquisitions, with the primary objective of deriving deformation information in the observed area. At Stromboli, this system operates in the Ku-band (17.0–17.1 mm) with a revisit time of 6–7 min and uses a 30-min image averaging process to improve the

signal-to-noise ratio (Di Traglia et al. 2021). The process of generating displacement maps, such as interferograms or cumulative displacement maps, involves a resampling procedure that results in images with a pixel size of approximately 2 ms along both the range and cross-range. Utilising a pixel-by-pixel stacking algorithm, it becomes possible to reconstruct cumulative displacement, incorporating coherence (>0.5) and a power filter (55 dB). This approach facilitates the tracking of displacement time series for selected points (averaged over pixels), providing a displacement measurement precision of 0.5 mm (Di Traglia et al. 2021).

Topographic surveys and change detection analysis

To estimate the volumetric changes resulting from the crater rim collapses that took place on Stromboli on 9 October and 4 December 2022, multiple topographic surveys were conducted using various remote sensing platforms. Specifically, the changes in topography were estimated by comparing digital elevation models (DEMs) derived from unmanned aircraft system (UAS) and single-pass synthetic aperture radar (sar) airborne data.

UAS-based topographic surveys were conducted on 15 and 16 December 2022 using a DJI Matrice 300 RTK with Zenmuse P1 camera (full-frame CMOS 45MP sensor, 84° field of view (FOV), 24-mm focal length lens). A predefined multi-flight mission was designed with a constant altitude of 250 m above ground level, 80% forward and side overlap, nadir camera orientation and a flight speed of 12 m/s. The camera's digital ISO, aperture and shutter speed were adjusted according to ambient light conditions. Data on camera position were collected using GNSS-RTK information embedded in the image metadata. Georeferenced images were then processed using the Agisoft Metashape software package (version 2.0.3) based on the structure-from-motion and multi-view stereo photogrammetry algorithm (SfM-MVS; James and Robson 2012). For additional details on the photogrammetric workflow, refer to Civico et al. (2021, 2022) and Schmid et al. (2021).

The analysis carried out with airborne (SAR) data is based on the exploitation of the classical SAR Interferometry (InSAR) technique, which allows generating the DEM of the observed area (Franceschetti and Lanari 1999; Rosen et al. 2000). In particular, we have exploited single pass (SP) InSAR data (Franceschetti et al. 1999; Rosen et al. 2000) with the aim of obtaining highly coherent interferograms suitable to generate accurate DEMs of the observed area. Specifically, we have used the SP InSAR data acquired during two airborne campaigns conducted before and after the 9 October 2022 event. In particular, we have generated a pre-event and a post-event DEM of the observed area and compared them to retrieve the co-eruptive topographic variations that occurred. It is highlighted that we have not exploited repeat-pass interferograms, thus overcoming the limitations of the differential SAR Interferometry (DInSAR) technique (Massonnet et al. 1993; Franceschetti and Lanari 1999; Rosen et al. 2000), that in this case does not allow carrying out effective co-eruptive analyses with the available spaceborne as well as airborne SAR data. This is due to the abrupt reduction of the interferometric coherence of the co-event repeat-pass SAR interferograms relevant to the phenomenon at hand. On the other hand, it must be stressed that with the applied methodology, based on the generation of SP InSAR DEMs of the observed area, the achievable accuracy of the retrieved co-event topographic variations is worse than the sub-centimetre accuracy that we would have obtained if the DInSAR technique had been successfully implemented (Casu et al. 2006). Indeed, the vertical accuracy of SP InSAR DEMs, which is not uniform over the observed area and depends on both the geometric and electromagnetic characteristics of the SAR interferometer (Franceschetti et al. 1999; Rosen et al. 2000), is typically on the order of the metres (Rodriguez 2006; Perna et al. 2016; Rizzoli et al. 2017). For the SP InSAR DEMs generated in our case, the corresponding vertical accuracy map is provided in the Online Resources. For the present analysis, we have used the archive of X-band SP InSAR data collected by the airborne SAR infrastructure available at the Institute for Electromagnetic Sensing of the Environment (IREA)-National Research Council of Italy (CNR), Naples, Italy (Esposito et al. 2024). From the archive, we extracted data acquired during the 12 September and 17 October 2022 campaigns with the MIPS system (Natale et al. 2022), which is based on the FMCW technology and operates at X-band with a SP InSAR configuration. The system was mounted on a Cessna 172, and the SP InSAR configuration was obtained by placing the radar antennas on the right wing strut (Natale et al. 2022). The volcano was observed by the radar from different view angles in order to reduce shadowing and clutter effects in mountainous areas (Esposito et al. 2023; Franceschetti and Lanari 1999). Specifically, the area was illuminated using two flight circuits, say C1 and C2, each consisting of four straight tracks, to counteract shadowing effects, particularly on the northwest flank (see Fig. S6 in the Online Resources for track description). Both circuits were flown twice, except for C2 on 17 October 2022, which was flown once. Data acquisitions relevant to the same campaign were made on the same day, with a minimal time gap. This data redundancy improved the accuracy of the final DEM, as separate processing chains were applied to the data acquired from different flight tracks (Berardino et al. 2023; Esposito et al. 2024). Details of the acquisition method and accuracy estimate for each of the DEMs generated are given in the Online Resources.

DEM-to-DEM co-registration was based on the minimization of the root mean square (RMS) error between one

DEM and the other (e.g., Favalli et al. 2018). We followed the workflow outlined in Di Traglia et al. (2020). After the coregistration, the residual displacement ($\sigma_{\Delta Z}$) between the DEMs from September 9, 2022 to October 17, 2022, was 0.94 m, while the $\sigma_{\Delta Z}$ between the DEMs from October 17, 2022 to May 22, 2023, was 2.10 m. The volume (V) added or lost between two acquisitions was calculated from the DEM difference according to the formula $V=\Sigma_i \Delta x^2 \Delta z_i$ (where Δx is the grid step and Δz_i is the height variation within the grid cell i, calculated in a given area). The volume error was determined by the formula $Err_V=A\sigma_{\Delta Z}$, where A is the investigated area (Favalli et al. 2010).

Slope stability analysis

The stability analysis of the crater rim was performed using a 2D limit equilibrium method (LEM) with the slope stability analysis program (SSAP; Borselli et al. 2011; Borselli 2023). The aim of this analysis was to investigate the stress conditions of the slope and to understand the mechanisms that led to the destabilisation of the volcaniclastic deposits, ultimately triggering deposit-derived PDCs. The factor of safety (FS) for potential slip surfaces was assessed using a 2D LEM analysis by applying shear strength parameters based on different failure criteria. This analysis used the same approach as Di Traglia et al. (2023a, b), which had previously proved effective in replicating landslide events in the Sciara del Fuoco (30 December 2002) and the crater rim (6–7 August 2014 and 19 May 2021). The mechanical stratigraphy of the crater rim was represented by a set of geotechnical units (Table 2), including the following:

A shallow layer in the subaerial section of the slope, composed of volcaniclastic material with rockfill-like properties. For this layer, the analysis considered the generalised Hoek and Brown (GHB) criterion (Hoek et al. 2002; Hoek 2007; Hoek and Brown 2019; Heap et al. 2020) failure and the Barton-Kjaernsli (1981) and Barton (2013) non-linear failure envelope (B-K criterion) for the rockfill-like material in its local discontinuity with the local lava bedrock.

The lava-breccia unit, characterised by lava layers (comprising 35–65% of the total) interspersed with breccia material. This lithostratigraphic unit, originally proposed for rock masses with comparable percentages of lava and breccia components, was used as a lower boundary in the geotechnical characterisation of the volcanic structure. The GHB failure was also considered for this unit in combination with the B-K criterion, as implemented in Di Traglia et al. (2023a, b) previous analysis.

This analysis used precise topographic data from UAS surveys and ground displacement data from GBInSAR to constrain the model results. It involved a comparison of the modelled critical zone slopes (with the lowest FS) with the regions where movement was documented, corresponding to the events of crater rim collapse.

The influence of ground acceleration due to explosive activity was not included in the stability analyses, as it was previously shown by Di Traglia et al. (2023a, b) that for accelerations consistent with paroxysmal explosions, the effect on crater rim stability is almost negligible.

Results

Volcanic activity through daily observations and camera images

During the period studied, the eruptive activity consisted mainly of ordinary Strombolian explosions, showing

Table 2 Geomechanical parameters used in the LEM simulations according to parametrization of Di Traglia et al. (2023a, b). *UCS*, uniaxial compressive strength; *GSI*, Geological Strength Index; *mi*, fitting constant for intact rocks (controls the steepness and curvature of the failure envelope); *D*, disturbance factor; *γdry*, dry bulk volume; *γsat*, saturated bulk volume; *JRC*, joint roughness coefficient; *JCS*, joint wall compressive strength; *φr*, residual friction angle; *Lo*, length referred to 100-mm laboratory scale samples; *Ln*, length referred to in situ block sizes; *β*, inclination angle of discontinuities; *Δβ*, discontinuity angle range

Geomechanical parameters following the GHB (Hoek et al. 2002)							
Layer	UCS (MPa)	GSI (−)	mi (−)	D (−)	γdry (kN/m^3)	γsat (kN/m^3)	
Rock-fill (GHB- criterion)	40	30	19	0	19	22	
Lava Breccia (GHB- criterion)	40	30	19	0	19	22	
Barton and Kjaernsli (1981) criterion							
Layer	JRC (°)	JCS (Mpa)	*φr* (°)	*L*0 (m)	*L* (m)	*β* (°)	Δ*β*(°)
Rock-fill	20	10	32.00	1.00	150.00	40.00	20.00
Lava Breccia	20	20	32.00	1.00	150.00	40.00	20.00

variations in frequency and intensity. There were also lava overflows on 3 October, 9–17 October, 16 November and 4–8 December 2022. In two cases, these lava overflows were associated with crater rim failures, resulting in the development of deposit-derived PDCs on 9 October (Fig. 2) and 4 December 2022 (Figs. 3 and 4). The lava overflow event that occurred from 9 to 17 October 2022 was also associated with deposit-derived PDCs that originated directly from the volcaniclastic deposits on the SdF. The main features can be summarised as follows:

All overflows were preceded by an escalation of explosive activity, particularly marked by spattering from vents in the northern crater area;
The overflows on 3, 4 and 7 October and on 16 November 2022 were brief (lasting 6, 3, 3 and 5 h, respectively), travelling only a few hundred metres from the vent. These events were not associated with significant crater rim collapses, except for minor instances resulting mainly from the collapse of lava mixed with volcaniclastic debris along the SdF. During these events, a decrease in explosive activity was observed during the effusive phase;
The overflows of 9 October and 4 December 2022 were prolonged (days) and rapidly reached the coast. These two events were associated with significant crater rim collapses. During the 9 October 2022 overflow, no decrease in explosive activity was observed, while the decrease was documented as the effusive activity subsided (Fig. 2), whereas during the 4 December 2022 overflow, a significant decrease in explosive activity was recorded in the *N* vents that emitted the flow. However, the CS area continued to produce explosions. The crater rim collapse on 4 December 2022 was the largest, occurring progres-

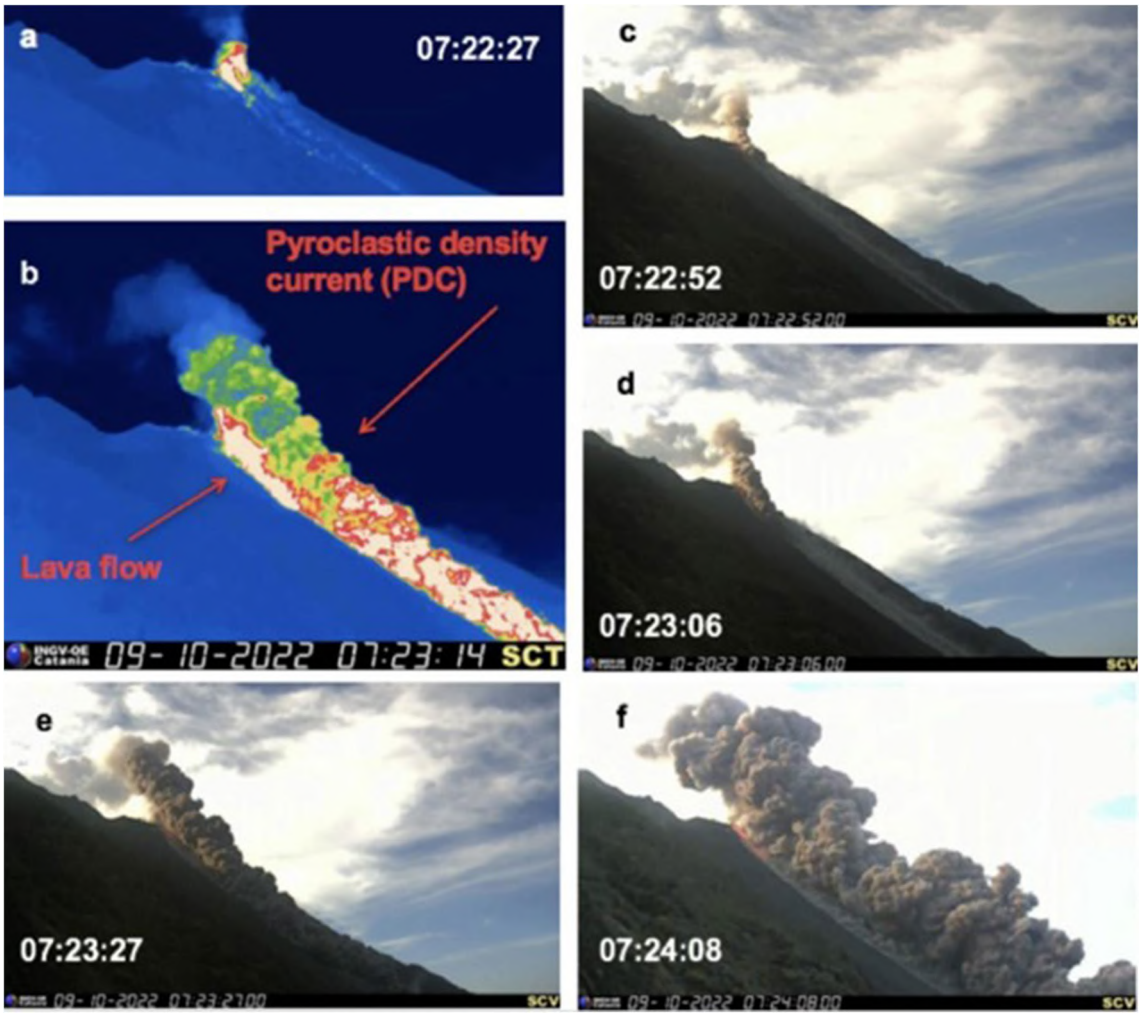

Fig. 2 Thermal images (**a**, **b**) from the SCT camera recorded on 9 October 2022 at 07:22:27 and 07:23:14, respectively, showing the initial failure of the NE crater rim (**a**) and the PDC spreading along the SdF (**b**). Visual images (**c**–**f**) recorded by the SCV camera between 07:22:52 and 7:24:08 showing the growing ash cloud expanding from the summit crater along the SdF slope

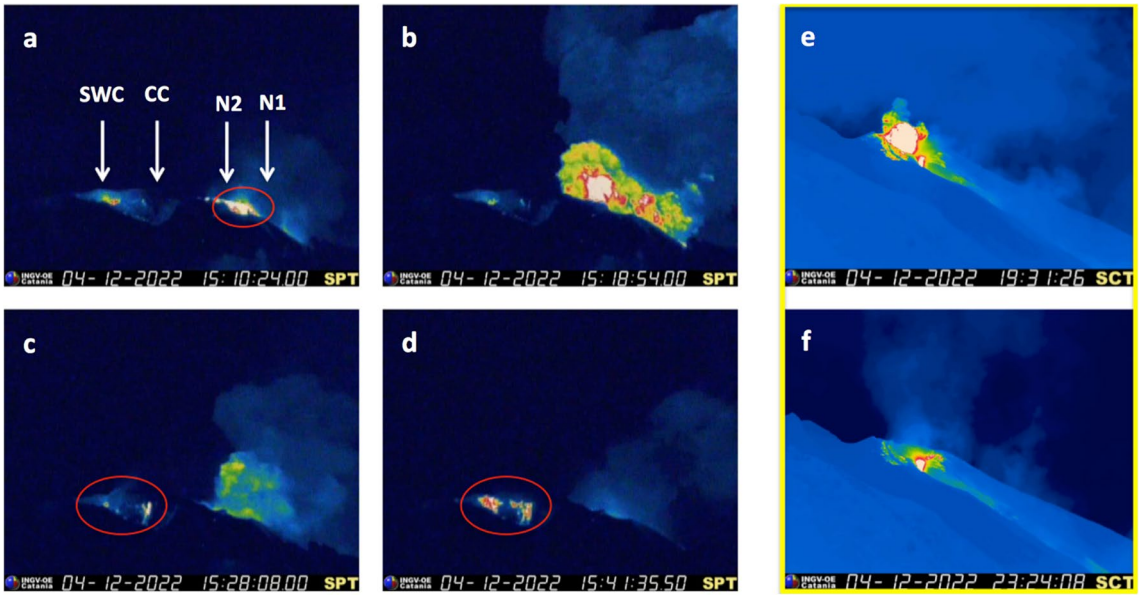

Fig. 3 Thermal images recorded from the SPT monitoring camera located at Il Pizzo Sopra La Fossa (**a**–**d**) displaying the crater area from south and from a distance of ~ 250 m on 4 December 2022. The field of view is ~ 300 m wide. SWC, SW crater; CC, central crater; N1 and N2, vents from the NE crater zones. The comparison between a and b shows the portion of N1 (red circle in **a**) that failed. **b** In white-yellow, the pyroclastics and in blue the ash cloud rising from the failed crater. The red circles in **c** and **d** display the landslides occurring within the north inner crater wall of SWC as a result of the drainage of the upper conduit. **e**, **f** Thermal images from the SCT camera located on the north rim of the Sciara del Fuoco showing the crater area from NE, with an explosion from N1 (**e**) and lava flow output (**e**, **f**) within the saddle excavated by the slope failure

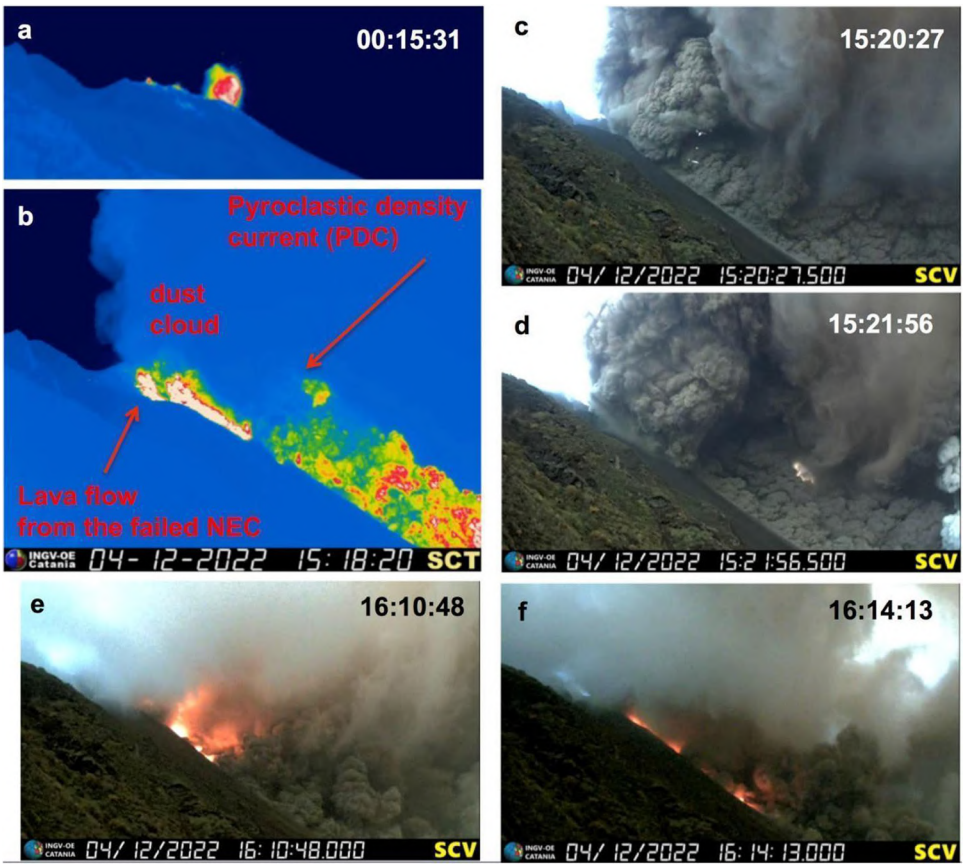

Fig. 4 **a**, **b** Thermal images recorded from the SCT camera located on the north rim of the Sciara del Fuoco (see Fig. 1b for camera location) showing the crater area from NE on 4 December 2022 (**a**–**b**), with a an explosion from SWC and a hornito at the NEC crater rim at 00:15:31, before the failure. **b** Lava flow (white portion) output at 15:18:20 after the NEC failure spreading within the saddle excavated by the failure and pyroclastic density current (PDC) forming a dust cloud above the crater. **c**–**f** Visible images from the SCV camera showing the spreading of a pyroclastic density current along the Sciara del Fuoco with lightnings (**c**, **d**) and a lava flow (**e**, **f**). All times are UTC

sively with a total duration of over 1 h (14:10 –15:18; Figs. 3 and 4).

Detailed descriptions of the events can be found in the Online Resources.

Seismic data

The data analysed were collected at the STRA station, located near the summit craters (Fig. 5); the station is equipped with a Guralp CMG40T broadband seismometer with a sampling rate of 50 samples per second. The east–west component of the STRA station was chosen for analysis as it is more representative of the craters' activity and related phenomena (Giudicepietro et al. 2020). Additionally, this component is sensitive to signals generated by surface sources such as rolling landslides. A spectral analysis of seismic signals generated by lava overflow events, followed by crater collapse and the formation of PDC, was conducted on events occurring on 9 October and 4 December 2022 (Fig. 5). The time series of RSAM (real-time seismic amplitude measurement) was calculated using a 1-min window and compared between two frequency ranges. The first range (Fig. 5a, b), which was from 1 to 7 Hz, is characteristic of spattering, summit tremors and explosive activity

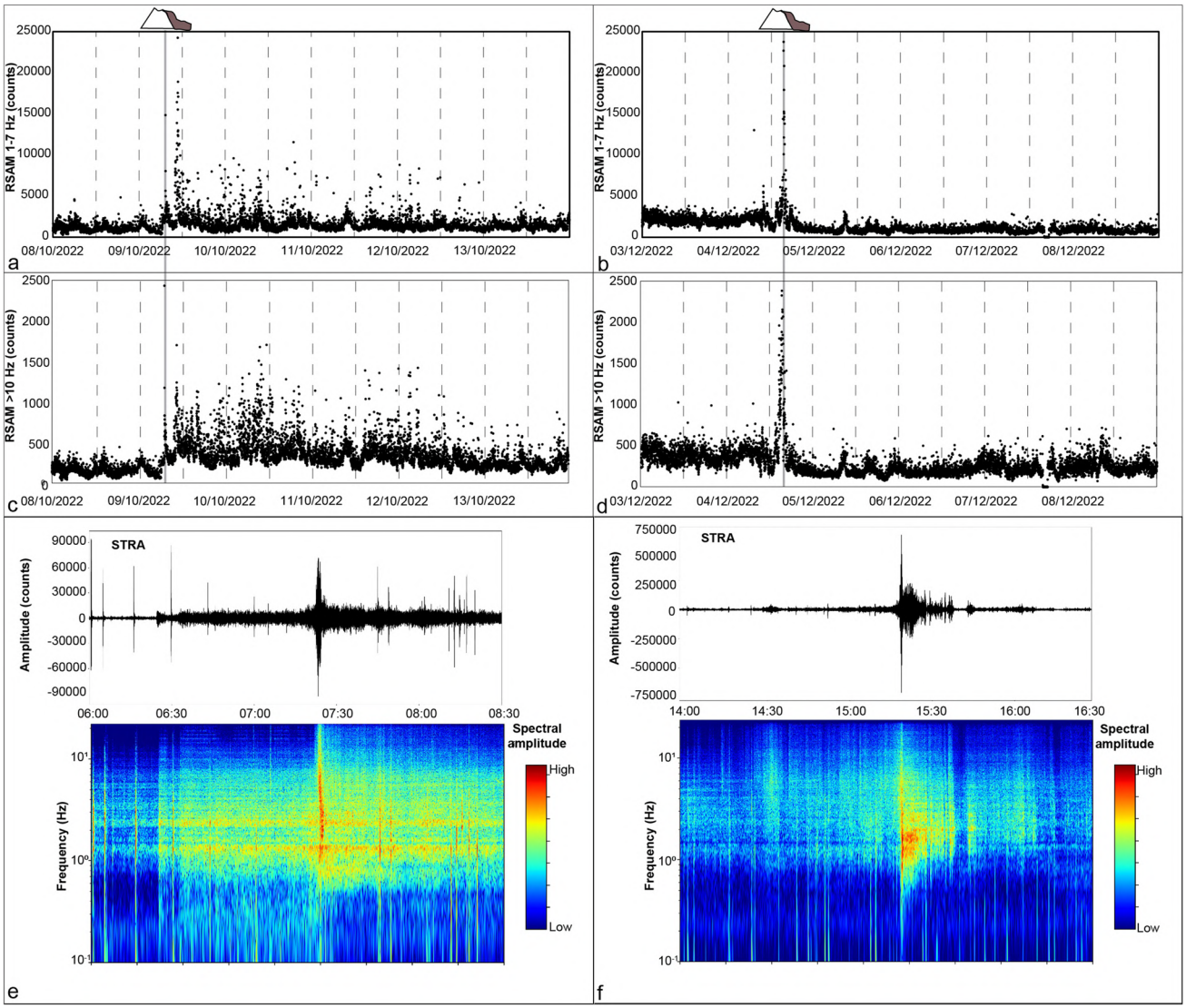

Fig. 5 Analysis of the seismic amplitude and spectral content of the STRA station signal, east–west component. **a** RSAM in the 1–7 Hz frequency range for the days between 8 and 13 October 2022. **b** RSAM in the 1–7 Hz frequency range for the days between 3 and 8 December 2022. **c** RSAM of the high-pass filtered seismic signal (> 10 Hz) for the days between 8 and 13 October 2022. **d** RSAM of the high-pass filtered seismic signal (> 10 Hz) for the days between 3 and 8 December 2022. **e** Seismogram of the event on 9 October 2022, with the corresponding spectrogram. **f** Seismogram of the event on 4 December 2022, with the corresponding spectrogram

at the craters, excluding gas explosions, as previously found in works such as Giudicepietro et al. (2022, 2023). The frequency band > 10 Hz (Fig. 5c, d) is particularly responsive to the rolling of blocks on the SdF, emphasising the occurrence of landslides and the detachment of blocks from the lava overflow front (Esposito et al. 2006). RSAM was performed for the first event between 8 and 13 October 2022 (Fig. 5a, c), and for the second event between 3 and 8 December of the same year. In the RSAM relevant to the event on 9 October 2022, the amplitude in the > 10 Hz band remains high for several days after the event, until around 13 October 2022 (Fig. 5c). This is likely due to the erosion along the SdF by overflows and PDCs. In relation to the event on 4 December 2022, a notable increase in frequency range signals was detected, specifically in the > 10 Hz and 1–7 Hz ranges, solely during the event (Fig. 5b, d). Subsequently, the seismic amplitude returned to low levels in the following days. The spectrograms of the event on 9 October 2022 (Fig. 5e) show a variation in frequency content after the event lasting for at least an hour, which is also indicative of landslides on the SdF. In contrast, the 4 December 2022 event shows that the characteristics of the seismic signal return to pre-event conditions a few minutes after the collapse of the crater (Fig. 5f).

Ground deformation

In general, measurements of ground deformation exhibit cycles of progressively increasing displacements towards the sensor until the onset of overflows, followed by movements away from the sensor after the overflows. The approaching and receding movements, although of different magnitudes and rates, are all centred on the northern vents. A clear deviation from this pattern was observed during the overflow and subsequent collapse of the crater rim on 9 October 2022 and 4 December 2022 (Fig. 6). In this case, the pre-event interferograms revealed a deformation geometry that was no longer centred on the northern vents. Instead, they showed interferometric fringes consistent with lateral movement along the slope, indicating crater rim sliding. During the 9 October 2022 event, the lateral movements along the slope were very similar to those centred on the N2 vent. Figure 6 a shows the interferometric fringes slightly diverging towards the NW, with a recorded movement of about 6 mm per hour. However, during the event on 4 December 2022, the lateral movement along the slope was more extensive, covering a larger area at a rate of about 32 mm over 2 h (maximum displacement rate: 16 mm/h; Fig. 6b).

Volumes of the collapses

The differences between the data acquired on 12 September 2022 (airborne SAR) and 17 October 2022 (airborne SAR) allowed us to calculate a conservative estimate of the volume of the crater rim collapse on 9 October 2022, at approximately $6.4 \pm 1.0 \times 10^3$ m^3 (Fig. 7a). In addition to crater rim failure, the crater terrace is also affected by vertical collapse (pit crater formation), which is common on Stromboli in association with overflows (Calvari et al. 2014; Di Traglia et al. 2014a) and lava flows (Casagli et al. 2009; Valade et al. 2016). On the other hand, comparing the data from 17 October 2022 (airborne SAR) with that of 22 May 2023 (UAS) enabled us to estimate a minimum volume of the collapse that took place on 4 December 2022, amounting to approximately $88.9 \pm 26.7 \times 10^3$ m^3 (Fig. 7b). It is crucial to note that these estimates are conservative, as the volcano's activity continued post-collapse, leading to the swift accumulation of materials within the detachment zones, as evidenced by video surveillance data. The topographic change detection also allowed us to estimate the volume eroded in the SdF as a result of the overflows generated between 9 and 15 October 2022, equal to $1.88 \pm 0.08 \times 10^6$ m^3 (Fig. 7a).

Crater rim stability

A 2D stability analysis using the LEM was conducted, with SSAP software using the techniques presented in Di Traglia et al. (2023a, 2023b), to assess the stability of the crater rim on 9 October 2022 along the A-A′ profile (Fig. 8a, c). Similarly, the stability of the crater rim on 4 December 2022 was quantified by applying the LEM analysis along the B-B′ profile (Fig. 8b, d). The stability analysis of both profiles shows that the volcaniclastic accumulations were in metastable conditions with diffuse instability (FS close to 1.0 or < 1.0). The modelling results were compared with the ground displacement data recorded by the GBInSAR system (Fig. 8c, d). This comparison not only revealed the variation in recorded deformation but also helped identify correspondences between mobile areas and regions with lower FS. The significant difference in volume between the December event and that of October can be explained by both the magnitude of the thrust that caused the collapse and the irregular topography present at the time of the collapse on 4 December 2022.

Discussion

The collapse events of 9 October 2022 and 4 December 2022 involved approximately $0.06 \pm 0.01 \times 10^5$ m^3 and $0.89 \pm 0.27 \times 10^5$ m^3, respectively, of volcanic debris situated on the northern edge of the crater area. As a point of comparison (Fig. 9), the volumetric estimates of the crater rim collapse that occurred on 19 May 2021, linked to the overflow commencing at the same time and lasting for 4 days (Calvari et al. 2022; Di Traglia et al. 2022), were at a

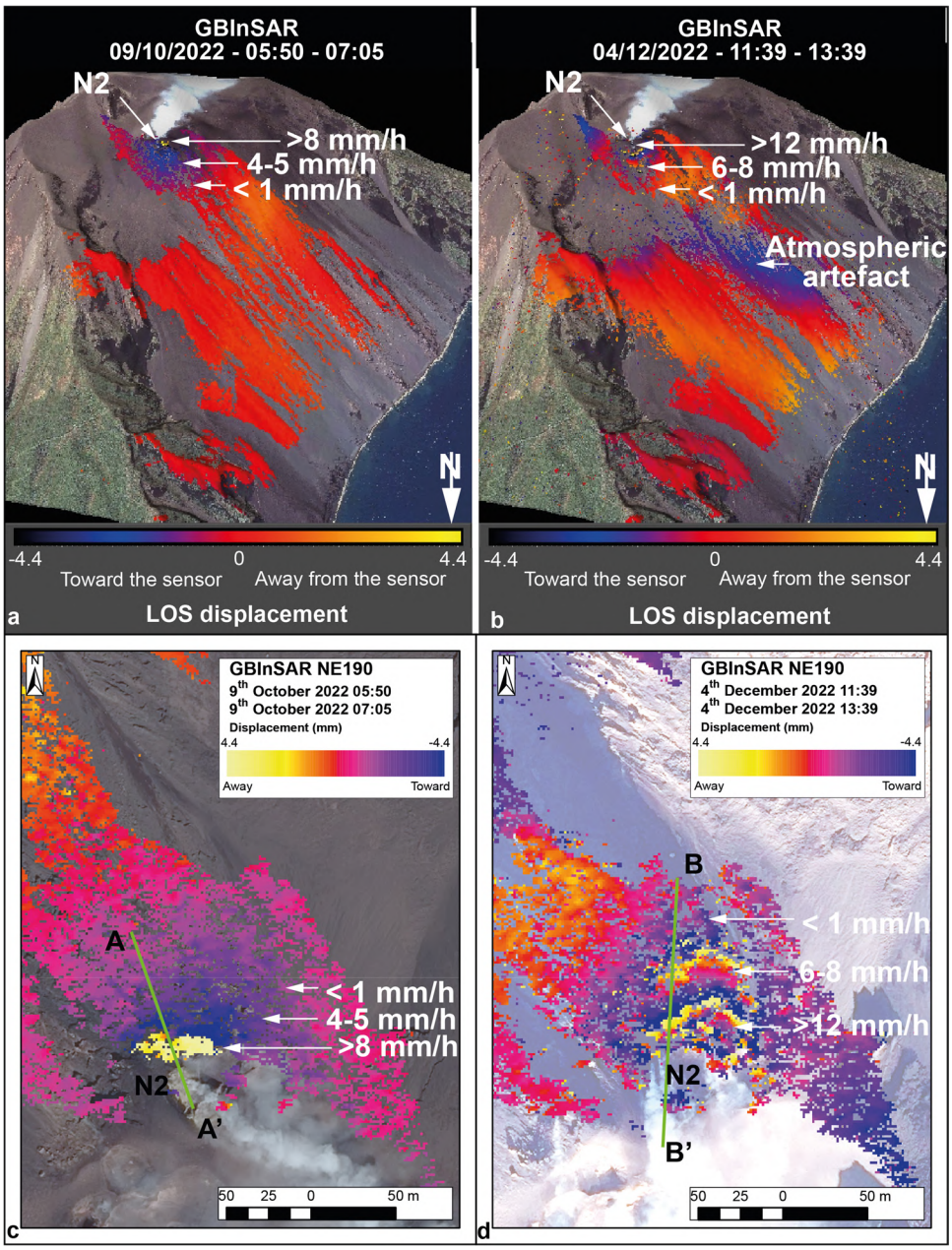

Fig. 6 **a**, **b** Side views from north and **c**, **d** plan views (north is up) of Stromboli volcano. Ground displacement observed on **a** and **c** 9 October 2022 (05:50–07:05) and **b** and **d** 4 December 2022 (11:39–13:39). In **c** and **d**, the A-A′ and B-B′ profiles used in the stability analysis (Fig. 8) are shown

minimum volume of $0.44 \pm 0.03 \times 10^5$ m^3 (Casalbore et al. 2022). These values place the Stromboli events between those of medium and low volume compared to those estimated for the other deposit-derived PDCs worldwide (see Table 3).

The mechanism of formation of deposit-derived PDCs formed by crater rim failure, termed Arenal-type PDCs by Alvarado and Soto (2002), may be similar to that proposed by Sato et al. (1992) for gravitational dome collapse PDCs, termed Merapi-type. This type of dome-collapse PDCs would form through the gravitational crumbling of the lava dome (Sato et al. 1992). In accordance with this framework, the triggering mechanisms of crater rim failure and PDC generation must also be sought within the processes leading to the surpassing of the tensile strength of hot volcaniclastic deposits and agglutinates, likely to be induced by the magma thrust in the occurrence of lava overflows. By comparing observations from Stromboli and other volcanoes, a general pattern emerges: (i) the inflation of the crater area and localised deformation on the slope, leading to subsequent collapses. This phenomenon is consistently observed in Stromboli (e.g. Casagli et al. 2009; Marchetti et al. 2009; Di Traglia et al. 2014b, 2018a, 2018b, 2018c, 2018d, 2023a) and precedes crater rim collapse events at Arenal volcano (Alvarado and Soto 2002; Cole et al. 2005), and it is associated with the growth of magmastatic thrust on the flank

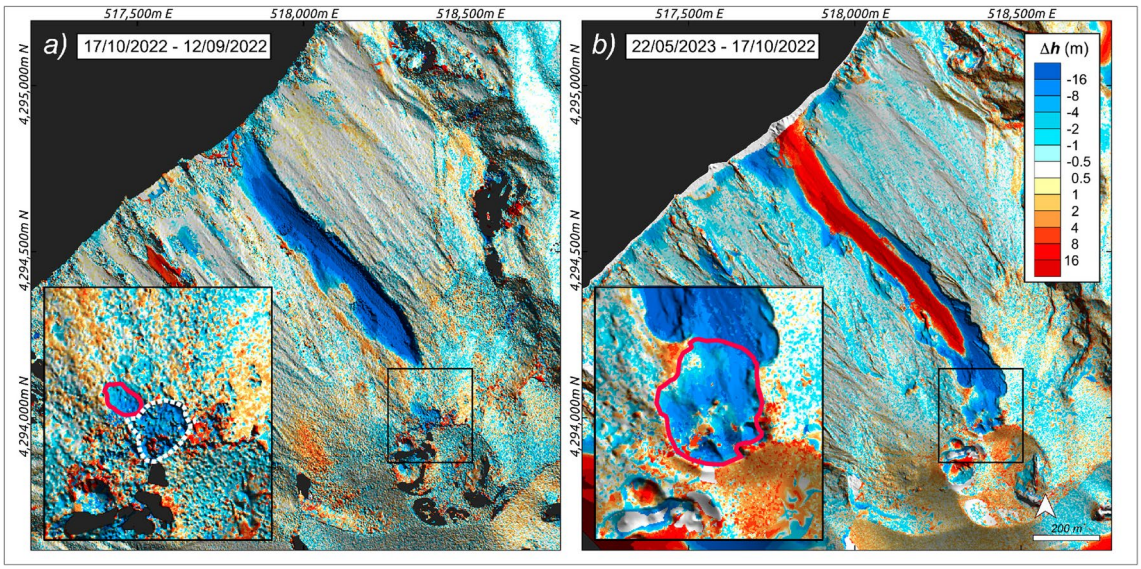

Fig. 7 **a** Analysis of the detection of topographic changes between the airborne SAR DEMs of 12 September 2022 and 17 October 2022. It is possible to observe the strong erosion in the SdF area due to the overflows and PDC activity. The inset shows the zoom of the NEC area to observe the detachment area associated with the 9 October 2022 crater rim failure. The collapsed area during the crater rim failure is indicated by the red line, and the dashed white line indicates the pit-crater area. In **b**, the differences between the 17 October 2022 airborne SAR DEM and the 22 May 2023 UAS DEM are shown, highlighting both the detachment area of the 4 December 2022 crater rim failure (seen in detail in the inset, red line) and the filling of the canyon in the SdF by overflows and volcaniclastic accumulation

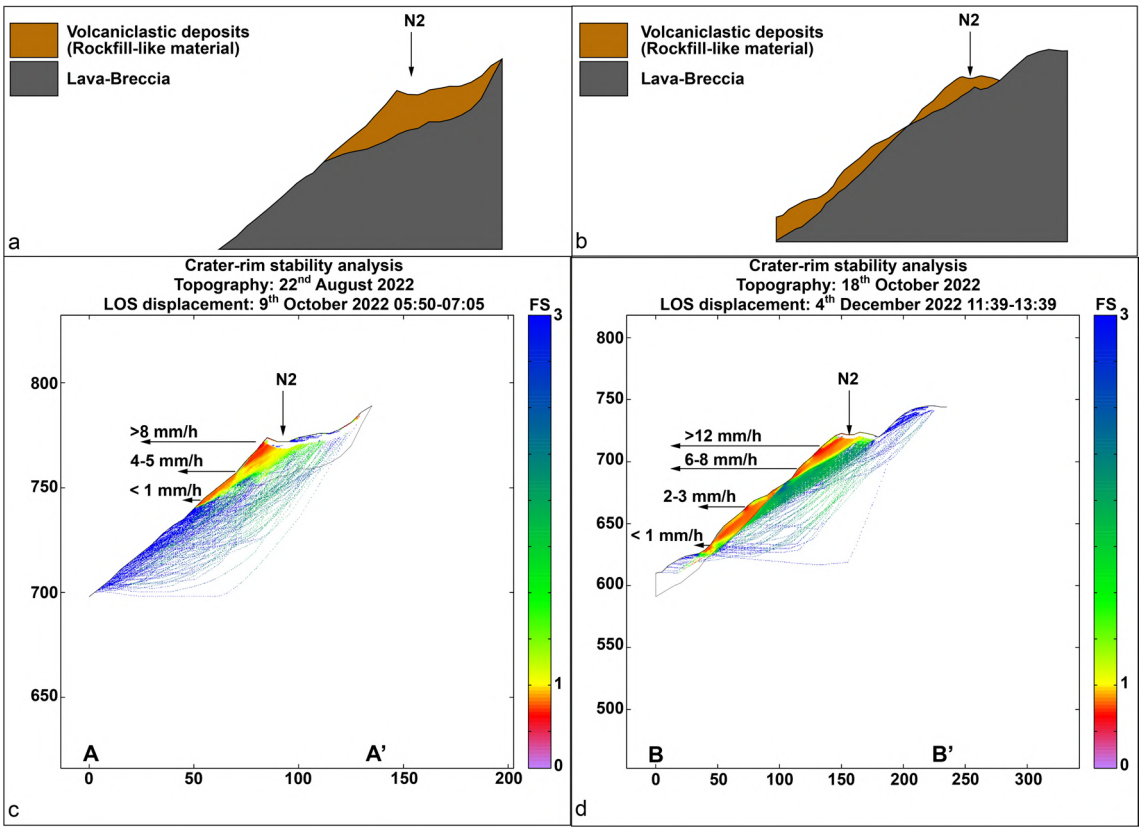

Fig. 8 The geological-technical model of the crater rim is presented in A-A′ (**a**) and B-B′ (**b**) profiles (see profile track in Fig. 6). Results from the 2D stability analysis depict the distribution of the factor of safety (FS) in the examined A-A′ (**c**) and B-B′ (**d**) profiles

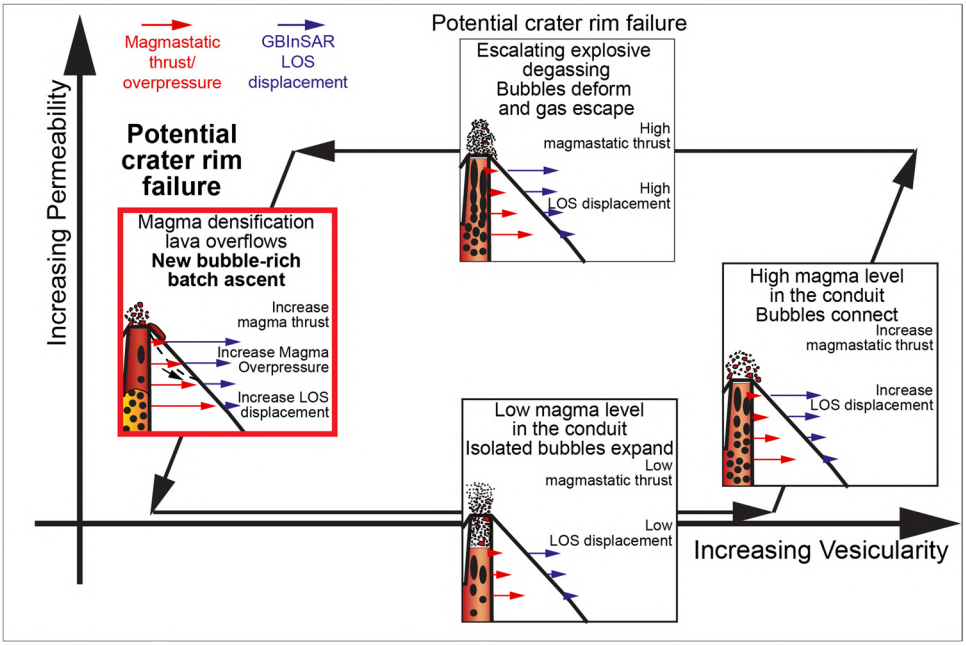

Fig. 9 Schematic model of crater rim failure triggering in relation to hysteresis in magma permeability–porosity path (see Rust and Cashman 2011 and Cashman and Sparks 2013). The 9 October and 4 December 2022 failure were triggered by the prompt arrival of a magma batch rich in gas bubbles that generated the overpressure essential for triggering the crater rims

Table 3 Remobilized volumes (estimated with different methods) relating to different episodes of deposit-derived PDCs. Data from Imbò (1949), Cole et al. (2005), Lube et al. (2007), Kelfoun et al. (2009), Norini et al. (2009), Bernard et al. (2014), Di Roberto et al. (2014), Andronico et al. (2018), Albino et al. (2020), Calvari et al. (2022), Casalbore et al. (2022), Di Traglia et al. (2022), Charbonnier et al. (2023) and this work

Volcano	Date	Volume	References
Arenal (Costa Rica)	Post-1968 deposit-derived PDCs	$\sim 0.5 \times 10^6$ m^3 (average)	Alvarado and Soto (2002); Cole et al. (2005)
Arenal (Costa Rica)	28 August 1993	$2.2 \pm 0.8 \times 10^6$ m^3	Alvarado and Soto (2002)
Arenal (Costa Rica)	23 August 2000	$\sim 2 \times 10^6$ m^3	Alvarado and Soto (2002)
Etna (Italy)	16 November 2006	$0.35 \pm 0.05 \times 10^6$ m^3	Norini et al. (2009)
Etna (Italy)	11 February 2014	$1.06 \pm 0.36 \times 10^6$ m^3	Andronico et al. (2018)
Fuego (Guatemala)	3 June 2018	$22.5 \pm 7.5 \times 10^6$ m^3 (each flow ~ 3–8×10^6 m^3)	(Ferres and Escobar Wolf 2018; Naismith et al. 2019; Albino et al. 2020; Charbonnier et al. 2023)
Ngauruhoe (New Zealand)	February 1975	$\sim 1.6 \times 10^4$ m^3 (max volume)	Lube et al. (2007)
Ngauruhoe (New Zealand)	February 1975	$\sim 1.5 \times 10^3$ m^3 (min volume)	Lube et al. (2007)
Tungurahua (Ecuador)	2006 eruption	Total: $\sim 20 \times 10^6$ m^3 (each flow $\sim 0.1 \times 10^6$ m^3)	Kelfoun et al. (2009), Bernard et al. (2014)
Stromboli (Italy)	11 September 1930	$\sim 0.45 \times 10^4$ m^3	Di Roberto et al. (2014), Salvatici et al. (2016)
Stromboli (Italy)	19 May 2021	$0.44 \pm 0.03 \times 10^5$ m^3	Casalbore et al. (2022)
Stromboli (Italy)	9 October 2022	$0.06 \pm 0.01 \times 10^5$ m^3	This work
Stromboli (Italy)	4 December 2022	$0.89 \pm 0.27 \times 10^5$ m^3	This work
Vesuvio (Italy)	March 1944	$\sim 0.3 \times 10^6$ m^3 (larger flow)	Imbò (1949)

of the summit cones (Di Traglia et al. 2023a,b); and (ii) an increase in seismic tremor from days to hours before the event, analogous to patterns observed prior to main effusive events on Stromboli (De Cesare et al. 2009; Di Traglia et al. 2018a; Giudicepietro et al. 2023). Regarding crater rim collapses that occurred at Stromboli, it is noteworthy the differences between overflow events that did not have associated failures of significant volumes and those that did. All the events were preceded by an escalation in explosive activity, particularly spattering from the vents in the N area. While a decline in explosive activity was documented during the overflows on 3, 4, 7 October, and 16 November 2022, no significant reductions in explosive activity were observed during the effusive phase for the events on 9 October and

4 December 2022. There was only a brief interruption of explosions from the northern area during the collapse on 4 December 2022, attributed to morphological-structural variations induced by the collapse itself (formation of a notable scar with conduit exposure). However, these variations were transient and explosive activity quickly resumed.

The concomitant increase in seismic tremor and deformation within the crater region of Stromboli has been interpreted as indicative of mass ascent of magma and gas (Di Traglia et al. 2014c). Volcanic tremor at Stromboli is mainly associated with a continuous quiescent degassing process. In particular, it is associated with the intermittent bursting of small (< 1 m) bubbles at the surface of the magma column, a phenomenon known as gas puffing (Ripepe and Gordeev 1999). This correlation is supported by the shallow depth of the tremor source (Saccorotti et al. 1998). In open-vent volcanoes, explosive processes result from rapid degassing (Aiuppa et al. 2020; Laiolo et al. 2022; Acocella et al. 2024). Subtle deformation of the volcanic edifice is associated with rapid degassing, as observed prior to the paroxysmal/basaltic Vulcanian explosions on Stromboli (Ripepe et al. 2021; Di Traglia et al. 2021). In contrast, the relatively slow ascent of the magmatic column over days, weeks or months produces deformation at a slower rate, ranging from millimetres per day to millimetres per hour (Di Traglia et al. 2015; 2018a). At Stromboli, the relationship between the deformation of the crater terrace, the amplitude of the tremor and the intensification of spattering activity suggests that changes in the magma level are associated with an increase in magma vesiculation, indicating increased explosive degassing activity (Colò et al. 2010; Giudicepietro et al. 2023). These phenomena typically precede the onset of effusive activity (Valade et al. 2016; Di Traglia et al. 2015; 2018a). This process likely led to an increase in magma density within the conduit (Fig. 9), following the model proposed by Rust and Cashman (2011) and Cashman and Sparks (2013). These models propose a vesiculation-densification model of magma that follows the hysteresis in the magma permeability–porosity path (see Rust and Cashman 2011; and Cashman and Sparks 2013). Expansion in isolated bubbles causes a rise in the magma column in the Stromboli conduit, which continues until the percolation threshold is reached (~60% vesicularity; Burton et al. 2007; Bourgisser et al. 2017; Colombier et al. 2021; even if this limit may be lower in the crystallised HP Stromboli magma). This leads to an increase in magma pressure in the conduit, causing a thrust on the crater rim, as indicated by the increase in measured displacement. At the same time, there is a shift from explosive activity with an abundant ash fraction to activity characterised by the deposition of abundant spatter. Subsequently, permeability increases up to a threshold that limits further expansion. In this phase, there is an escalation of explosive degassing with strong spattering activity without an increase in magmatic pressure (displacement remains high without further increase). During this phase, small crater rim failures can occur due to the accumulation of agglutinates on very steep slopes. This gas loss phase results in the densification of the magma and facilitates the generation of overflows at the expense of explosive activity. The result is increased magmastatic pressure within the conduit. As shown by Di Traglia et al. (2023a), the magmastatic thrust resulting from magma densification alone is insufficient to induce the collapse conditions of Stromboli's crater rim; an additional thrust is required. The slope stability simulation was used to investigate the magma thrust required to destabilise slip surfaces similar to those involved in the crater rim failures of 9 October and 4 December 2022, following the methodology of Di Traglia et al. (2023a, b a,b). The analysis reveals that destabilising the rim required a minimum thrust of 75 MN/m for the 9 October 2022 event and 150 MN/m for the 4 December 2022 event. Given the dense rock equivalent (DRE) density of 2750 kg/m^3 for Stromboli magma (Barberi et al. 1993), the magmastatic thrust, assuming completely dense magma, ranges from 5 to 10 MN/m, depending on the length of the tension crack at the surface top. For comparison, the thrust required for the 19 May 2021 crater rim collapse was about 2–3 MN/m, equal to or slightly greater than the magmatic thrust, while for the 7 August 2014 collapse, it was about 20–25 MN/m. The thrust required to trigger the deep landslide on 30 December 2002 was about 370–400 MN/m. These observations indicate that the overpressure responsible for generating the magmatic thrust that led to the crater rim failures on 9 October and 4 December 2022 was higher than that which triggered the onset of the 2014 flank eruption. This underlines the importance of the events on Stromboli in late 2022. The association of events leading to the collapse of the crater rim with the effusive phases and associated explosive activity suggests a relationship between these failure events and the supply of magma and gas. In particular, when a batch of densified magma is followed by a batch of magma that is still "bubble-rich" and has not been "densified" by the explosive degassing process, the overpressure that can develop in the upper part of the conduits can generate a magmatic thrust sufficient to trigger the failure of volcaniclastic rocks around the crater rim, with volumes on the order of 10^3–10^5 m^3. The "bubble-rich" magma batches are likely to sustain the Strombolian activity, while the denser upper part contributes to the lava overflow (e.g. Pioli et al. 2009). The pressure increase (revealed by increase in pre-effusive ground displacement) generates an additional magmastatic thrust, which is capable of triggering both overflows and crater rim failure. Magma thrust within the craters may have propagated towards the crater rim by bulbous bulging, as observed in some cinder cones (Petronis et al. 2013) and hypothesised for the Arenal (Alvarado and Soto 2002; Cole et al. 2005) and Etna (Behncke et al. 2008) crater rim failure, or by dike intrusion (Acocella et al. 2006; Acocella 2021). While the latter hypothesis is consistent with deformation data observed during the onset of

effusive eruptions at Stromboli (Casagli et al. 2009; Di Traglia et al. 2018a), no deformation patterns associated with planar structures are observed for the crater rim failure. Therefore, a "bulbous bulging" type of thrust is more likely in this context, as already shown by analogue models of Nolesini et al. (2013).

Once the magma has been evacuated from the upper part of the conduit, a new cycle is initiated by the decompression of new magma batches and their increased vesicularity. This process continues until the input rate from depth is sufficient to sustain the phenomenon. The phenomena that occurred on 4 December 2022 seem to be dominated by the instability of the crater area, resulting in multiple collapses affecting larger areas and volumes. Based on instability models, this can be explained by the increase in magma thrust from the conduit towards the crater rim, as well as by the morphology of the crater area, which has been significantly altered by previous events. In particular, the failure of 9 October 2022 and the formation of a canyon within the SdF due to erosive processes and landslides associated with the overflows of 9–15 October 2022 destabilised the entire summit area.

Recent rheological studies have shown that magmas from Stromboli volcano have a significantly reduced susceptibility to syn-eruptive nanolite crystallisation (Scarani et al. 2022). As a consequence, at Stromboli paroxysmal events and basaltic Vulcanian explosions, typically associated with significant increases in viscosity and probably delayed vesiculation (Rivalta et al. 2013), are less easily achieved (Valdivia et al. 2023). This explains why effusive phases anticipated by strong explosive degassing (Di Traglia et al. 2014c, 2018a; Valade et al. 2016; Giudicepietro et al. 2023), characterised by efficient bubble coalescence and gas percolation (Rust and Cashman 2011; Cashman and Sparks 2013), are more common than highly explosive events (Bevilacqua et al. 2020; Calvari and Nunnari 2023).

A mechanism similar to the one proposed, although not universally applicable, can serve as a guiding framework for future research efforts aimed at understanding the processes underlying the increase in magmastatic pressure that drives the magma necessary for crater rim collapse observed in other contexts, such as the crater rim collapses at Arenal volcano (Alvarado and Soto 2002; Cole et al. 2005) and Rincon de la Vieja (Baez et al. 2024), or the summit cone failure at Mt. Etna volcano (Calvari and Pinkerton 2002; Behnke et al. 2008).

Conclusions

In this study, an exhaustive examination of data obtained from the multi-parametric monitoring network on Stromboli (Italy), encompassing video surveillance, seismicity and ground deformation data, along with remote topographic sensing data, has facilitated the correlation of events leading to the crater rim collapse occurred on 9 October and 4 December 2022. Key findings from the study include the following:

the failures resulted in the remobilisation of $6.4 \pm 1.0 \times 10^3$ and $88.9 \pm 26.7 \times 10^3$ m^3 of volcaniclastic material, respectively, propagating as PDCs along the SdF;
these events were characterised by a preparatory phase marked by an increase in magmatic pressure in the preceding weeks, correlating with an increase in displacement rate;
an escalation of explosive degassing was observed, indicated by spattering accompanied by seismic tremors in the hours preceding the collapse;
the described events were interpreted as an initial rise of the magma column due to the increase in magma vesicularity, followed by gas release. Subsequently, the degassing process induced magma densification, leading to increased thrust on conduit walls due to heightened magmastatic pressure; and
this phase coincided with crater rim collapse, often followed or accompanied by the onset of lava overflow phases.

The gravitational instability of hot material deposited during eruptive activity can generate glowing deposit-derived PDCs, travelling at high temperatures over hundreds of metres to several kilometres from the source; these events thus may pose catastrophic risks to areas near steep-slope volcanoes. Their occurrence often links with crater rim failure triggered by factors such as magma thrust. A mechanism similar to the one proposed here may illuminate similar phenomena in other volcanoes. This underscores the need for a comprehensive, multi-parametric approach integrating seismic, deformation and remote sensing data to understand these events.

Disclaimer

The contents of this paper represent the authors' ideas and do not necessarily correspond to the official opinion and policies of the Presidenza del Consiglio dei Ministri-Dipartimento della Protezione Civile.

Supplementary Information The online version contains supplementary material available at https://doi.org/10.1007/s00445-024-01761-5.

Acknowledgements We would like to express our gratitude to all the colleagues who have contributed to the monitoring efforts on Stromboli. FeDiT is particularly grateful to Dario Delle Donne, Rosella Nave and Mauro Rosi for constructive discussions on the Stromboli activity. This work was edited by Valerio Acocella and revised by Guido Giordano and Roberto Sulpizio, to whom we are grateful for

their corrections and suggestions. We also acknowledge the support of EPOS-RI, including the one obtained through the EPOS-Italia JRU.

Funding Open access funding provided by Istituto Nazionale di Geofisica e Vulcanologia within the CRUI-CARE Agreement. This research has benefited from the support from the following projects: "Convenzione B2 DPC-INGV 2022–2024, Stromboli"; INGV project Pianeta Dinamico 2023–2025-ORME; INGV project Reti Multiparametriche (Task A2); INGV Progetto Strategico Dipartimentale 2019 "UNO"; INGV Progetto Strategico Dipartimentale 2019 "FIRST"; Accordo tra Università degli Studi di Firenze e Presidenza del Consiglio dei Ministri-Dipartimento della Protezione Civile 2022–2024; Accordo tra IREA-CNR e Presidenza del Consiglio dei Ministri-Dipartimento della Protezione Civile 2022–2024 and Accordo tra IGAG-CNR e Presidenza del Consiglio dei Ministri-Dipartimento della Protezione Civile 2022–2024. Partly funded by the European Union–Next Generation EU, National Recovery and Resilience Plan Mission 4-Component 2. Project title: "Causes and consequences of deposit-derived pyroclastic density currents" (P20222BP7J). The SSAP software research and development was funded by CONAHCYT (Mexico): Proyectos Ciencia Basica: CB-2016/286764. SSAP2010 is FREEWARE software, i.e. it is distributed free of charge only at HTTPS://WWW.SSAP.EU.

Availability of data and material The data presented in the article can be requested to the authors by contacting the corresponding author federico.ditraglia@ingv.it. The data used in this study were provided by the INGV, UniFI, IGAG-CNR, UniRoma1 "La Sapienza" and by IREA-CNR. There is only one full version of the SSAP2010 software, and it is the free version that can be downloaded from the official website. The SSAP2010 User Licence allows the user unlimited use of the software with the ability to download all future updates from the web. SSAP20010 software is non-commercial software. Its distribution is non-profit (see SSAP User Licence).

Declarations

Competing interests The authors declare no competing interests.

References

Acocella V, Ripepe M, Rivalta E, Peltier A, Galetto F, Joseph E (2024) Towards scientific forecasting of magmatic eruptions. Nat Rev Earth Environ 5(1):5–22

Acocella V, Neri M, Scarlato P (2006) Understanding shallow magma emplacement at volcanoes: orthogonal feeder dikes during the 2002–2003 Stromboli (Italy) eruption. Geophys Res Lett 33(17).

Acocella V (2021) Volcano-tectonic processes. Advances in Volcanology Book Series, pp. XXVII, 552. Switzerland: Springer. https://doi.org/10.1007/978-3-030-65968-4

Aiuppa A, Bitetto M, Delle Donne D, La Monica FP, Tamburello G, Coppola D, Della Schiava M, Innocenti L, Lacanna G, Laiolo M, Massimetti F (2020) Volcanic CO2 tracks the incubation period of basaltic paroxysms. Sci Adv 7(38):eabh0191.

Albino F, Biggs J, Escobar-Wolf R, Naismith A, Watson M, Phillips JC, Marroquin GC (2020) Using TanDEM-X to measure pyroclastic flow source location, thickness and volume: application to the 3rd June 2018 eruption of Fuego volcano. Guatemala J Volcanol Geotherm Res 406:107063

Alvarado GE, Soto GJ (2002) Pyroclastic flow generated by crater-wall collapse and outpouring of the lava pool of Arenal Volcano. Costa Rica Bull Volcanol 63(8):557–568

Alvarado GE, Toulkeridis T, Miyabuchi Y, Pérez W (2023) Review of bomb and ash flows: genesis and case studies of a subset of block and ash flow deposits. Andean Geology 50(3):346–371

Andronico D, Di Roberto A, De Beni E et al (2018) Pyroclastic density currents at Etna volcano, Italy: the 11 February 2014 case study. J Volcanol Geotherm Res 357:92–105

Apuani T, Corazzato C, Cancelli A, Tibaldi A (2005) Stability of a collapsing volcano (Stromboli, Italy): limit equilibrium analysis and numerical modelling. J Volcanol Geotherm Res 144(1–4):191–210

Arrighi S, Principe C, Rosi M (2001) Violent strombolian and subplinian eruptions at Vesuvius during post-1631 activity. Bull Volcanol 63:126–150

Báez W, Alvarado GE, Sommer CA (2024) Complex facies architecture of unusual pyroclastic density current deposits at the Rincón de la Vieja Volcano. Costa Rica J Volcanol Geotherm Res 16:108030

Barberi F, Rosi M, Sodi A (1993) Volcanic hazard assessment at Stromboli based on review of historical data. Acta Vulcanol 3:173–187

Barton N (2013) Shear strength criteria for rock, rock joints, rockfill and rock masses: problems and some solutions. J Rock Mech Geotech Eng 5:249–261

Barton N, Kjærnsli B (1981) Shear strength of rockfill. J Geotech Eng Div 107:873–891

Behncke B, Calvari S, Giammanco S, Neri M, Pinkerton H (2008) Pyroclastic density currents resulting from the interaction of basaltic magma with hydrothermally altered rock: an example from the 2006 summit eruptions of Mount Etna, Italy. Bull Volcanol 70:1249–1268

Berardino P, Natale A, Esposito C et al (2023) On the time domain airborne SAR focusing in presence of strong azimuth variations of the squint angle. IEEE Trans Geosci Remote Sens 61:1–18

Bernard J, Kelfoun K, Le Pennec JL, Vallejo Vargas S (2014) Pyroclastic flow erosion and bulking processes: comparing field-based vs. modeling results at Tungurahua volcano. Ecuador Bull Volcanol 76:1–16

Bernard J, Eychenne J, Le Pennec JL, Narváez D (2016) Mass budget partitioning during explosive eruptions: insights from the 2006 paroxysm of Tungurahua volcano. Ecuador Geochem Geophys Geosyst 17(8):3224–3240

Bevilacqua A, Bertagnini A, Pompilio M et al (2020) Major explosions and paroxysms at Stromboli (Italy): a new historical catalog and temporal models of occurrence with uncertainty quantification. Sci Rep 10(1):17357

Beyreuther M, Barsch R, Krischer L, Wassermann J (2010) Obspy: a Python toolbox for seismology. Seismol Res Lett 81:530–533. https://doi.org/10.1785/gssrl.81.3.530

Borselli L, Capra L, Sarocchi D, De la Cruz-Reyna S (2011) Flank collapse scenarios at Volcán de Colima, Mexico: a relative instability analysis. J Volcanol Geotherm Res 208(1–2):51–65

Borselli L. (2023) SSAP 5.2 - Slope stability analysis program,. Manuale di Riferimento del Codice SSAP, Versione 5.2. Researchgate. https://doi.org/10.13140/RG.2.2.19931.03361

Bosman A, Casalbore D, Romagnoli C, Chiocci FL (2014) Formation of an 'a'ā lava delta: insights from time-lapse multibeam bathymetry and direct observations during the Stromboli 2007 eruption. Bull Volcanol 76:1–12

Burgisser A, Chevalier L, Gardner JE, Castro JM (2017) The percolation threshold and permeability evolution of ascending magmas. Earth Planet Sci Lett 470:37–47

Burton MR, Mader HM, Polacci M (2007) The role of gas percolation in quiescent degassing of persistently active basaltic volcanoes. Earth Planet Sci Lett 264(1–2):46–60

Cagnoli B, Romano GP, Ventura G (2015) Shaking of pyroclastic cones and the formation of granular flows on their flanks: results from laboratory experiments. J Volcanol Geotherm Res 306:83–89

Calvari S, Nunnari G (2023) Statistical insights on the eruptive activity at Stromboli volcano (Italy) Recorded from 1879 to 2023. Remote Sensing 15(19):4822

Calvari S, Pinkerton H (2002) Instabilities in the summit region of Mount Etna during the 1999 eruption. Bull Volcanol 63:526–535

Calvari S, Bonaccorso A, Madonia P et al (2014) Major eruptive style changes induced by structural modifications of a shallow conduit system: the 2007–2012 Stromboli case. Bull Volcanol 76:1–15

Calvari S, Intrieri E, Di Traglia F, Bonaccorso A, Casagli N, Cristaldi A (2016) Monitoring crater-wall collapse at active volcanoes: a study of the 12 January 2013 event at Stromboli. Bull Volcanol 78:1–16

Calvari S, Giudicepietro F, Di Traglia F, Bonaccorso A, Macedonio G, Casagli N (2021) Variable magnitude and intensity of Strombolian explosions: focus on the eruptive processes for a first classification scheme for Stromboli volcano (Italy). Remote Sensing 13(5):944

Calvari S, Di Traglia F, Ganci G et al (2022) Multi-parametric study of an eruptive phase comprising unrest, major explosions, crater failure, pyroclastic density currents and lava flows: Stromboli volcano, 1 December 2020–30 June 2021. Front Earth Sci 10:899635

Casagli N, Tibaldi A, Merri A et al (2009) Deformation of Stromboli volcano (Italy) during the 2007 eruption revealed by radar interferometry, numerical modelling and structural geological field data. J Volcanol Geotherm Res 182(3–4):182–200

Casalbore D, Romagnoli C, Chiocci F, Frezza V (2010) Morphosedimentary characteristics of the volcaniclastic apron around Stromboli volcano (Italy). Marine Geol 269(3–4):132–148

Casalbore D, Romagnoli C, Bosman A, Chiocci FL (2011) Potential tsunamigenic landslides at Stromboli volcano (Italy): insight from marine DEM analysis. Geomorphology 126(1–2):42–50

Casalbore D, Passeri F, Tommasi P et al (2020) Small-scale slope instability on the submarine flanks of insular volcanoes: the case-study of the Sciara del Fuoco slope (Stromboli). Int J Earth Sci 109:2643–2658

Casalbore D, Di Traglia F, Romagnoli C et al (2022) Integration of remote sensing and offshore geophysical data for monitoring the short-term morphological evolution of an active volcanic flank: a case study from Stromboli Island. Remote Sensing 14(18):4605

Cashman KV, Sparks RS (2013) How volcanoes work: a 25 year perspective. Bulletin 1;125(5–6):664–90.

Casu F, Manzo M, Lanari R (2006) A quantitative assessment of the SBAS algorithm performance for surface deformation retrieval from DInSAR data. Remote Sens Environ 102(3–4):195–210

Charbonnier SJ, Garin F, Rodríguez LA et al (2023) Unravelling the dynamics and hazards of the June 3rd, 2018, pyroclastic density currents at Fuego volcano (Guatemala). J Volcanol Geotherm Res 436:107791

Chiocci FL, Romagnoli C, Tommasi P, Bosman A (2008) The Stromboli 2002 tsunamigenic submarine slide: characteristics and possible failure mechanisms. J Geophys Res Solid Earth 113(B10).

Civico R, Ricci T, Scarlato P et al (2021) Unoccupied aircraft systems (UASs) reveal the morphological changes at Stromboli volcano (Italy) before, between, and after the 3 july and 28 August 2019 paroxysmal eruptions. Remote Sensing 13(15):2870

Cole PD, Fernandez E, Duarte E, Duncan AM (2005) Explosive activity and generation mechanisms of pyroclastic flows at Arenal volcano, Costa Rica between 1987 and 2001. Bull Volcanol 67:695–716

Colò L, Ripepe M, Baker DR, Polacci M (2010) Magma vesiculation and infrasonic activity at Stromboli open conduit volcano. Earth Planet Sci Lett 292(3–4):274–280

Colombier M, Vasseur J, Houghton BF, Cáceres F, Scheu B, Kueppers U, Thivet S, Gurioli L, Montanaro C, Soldati A, Di Muro A (2021) Degassing and gas percolation in basaltic magmas. Earth Planet Sci Lett 573:117134

Davies DK, Quearry MW, Bonis SB (1978) Glowing avalanches from the 1974 eruption of the volcano Fuego. Guatemala Geol Soc Am Bull 89(3):369–384

De Cesare W, Orazi M, Peluso R et al (2009) The broadband seismic network of Stromboli volcano. Italy Seismol Res Lett 80(3):435–439

Di Roberto A, Bertagnini A, Pompilio M, Bisson M (2014) Pyroclastic density currents at Stromboli volcano (Aeolian Islands, Italy): a case study of the 1930 eruption. Bull Volcanol 76:1–14

Di Traglia F, Intrieri E, Nolesini T et al (2014a) The ground-based InSAR monitoring system at Stromboli volcano: linking changes in displacement rate and intensity of persistent volcanic activity. Bull Volcanol 76:1–8

Di Traglia F, Nolesini T, Intrieri E, Mugnai F, Leva D, Rosi M, Casagli N (2014b) Review of ten years of volcano deformations recorded by the ground-based InSAR monitoring system at Stromboli volcano: a tool to mitigate volcano flank dynamics and intense volcanic activity. Earth-Sci Rev 139:317–335

Di Traglia F, Cauchie L, Casagli N, Saccorotti G (2014c) Decrypting geophysical signals at Stromboli Volcano (Italy): integration of seismic and ground-based InSAR displacement data. Geophys Res Lett 41(8):2753–2761

Di Traglia F, Battaglia M, Nolesini T, Lagomarsino D, Casagli N (2015) Shifts in the eruptive styles at Stromboli in 2010–2014 revealed by ground-based InSAR data. Sci Rep 5(1):13569

Di Traglia F, Calvari S, D'Auria L et al (2018a) The 2014 effusive eruption at Stromboli: new insights from in situ and remote-sensing measurements. Remote Sensing 10(12):2035

Di Traglia F, Nolesini T, Ciampalini A et al (2018b) Tracking morphological changes and slope instability using spaceborne and ground-based SAR data. Geomorphology 300:95–112

Di Traglia F, Nolesini T, Solari L et al (2018c) Lava delta deformation as a proxy for submarine slope instability. Earth Planet Sci Lett 488:46–58

Di Traglia F, Bartolini S, Artesi E et al (2018d) Susceptibility of intrusion-related landslides at volcanic islands: the Stromboli case study. Landslides 15:21–29

Di Traglia F, Fornaciai A, Favalli M, Nolesini T, Casagli N (2020) Catching geomorphological response to volcanic activity on steep slope volcanoes using multi-platform remote sensing. Remote Sensing 12(3):438

Di Traglia F, De Luca C, Manzo M, Nolesini T, Casagli N, Lanari R, Casu F (2021) Joint exploitation of space-borne and ground-based multitemporal InSAR measurements for volcano monitoring: the Stromboli volcano case study. Remote Sen Environ 260:112441

Di Traglia F, Fornaciai A, Casalbore D et al (2022) Subaerial-submarine morphological changes at Stromboli volcano (Italy) induced by the 2019–2020 eruptive activity. Geomorphology 400:108093

Di Traglia F, Borselli L, Nolesini T, Casagli N (2023a) Crater-rim collapse at Stromboli volcano: understanding the mechanisms leading from the failure of hot rocks to the development of glowing avalanches. Nat Haz 115(3):2051–2068

Di Traglia F, Calvari S, Borselli L et al (2023b) Assessing flank instability of Stromboli volcano (Italy) by reappraising the 30 December 2002 tsunamigenic landslides. Landslides 20:1363–1380

Endo ET, Murray T (1991) Real-time seismic amplitude measurement (RSAM): a volcano monitoring and prediction tool. Bull Volcanol 53:533–545. https://doi.org/10.1007/BF00298154

Esposito AM, Giudicepietro F, Scarpetta S, D'Auria L, Marinaro M, Martini M (2006) Automatic discrimination among landslide, explosion-quake, and microtremor seismic signals at Stromboli volcano using neural networks. Bull of the Seismol Soc Am 96(4A):1230–1240

Esposito C., Berardino P., Natale A. et al. (2023) Stromboli volcano topography variations retrieval through airborne single-pass SAR interferometry. International Geoscience and Remote Sensing Symposium 2023-IGARSS 2023.

Esposito C., Berardino P. Di Vincenzo et al (2024, accepted). The IREA-CNR airborne SAR infrastructure: state of the art and future perspectives. International Geoscience and Remote Sensing Symposium 2024 - IGARSS 2024.

Franceschetti G, Lanari R (1999) Synthetic aperture radar processing. CRC PRESS, New York

Giordano G, De Astis G (2021) The summer 2019 basaltic Vulcanian eruptions (paroxysms) of Stromboli. Bull Volcanol 83:1–27

Giudicepietro F, López C, Macedonio G, Alparone S, Bianco F, Calvari S, De Cesare W, Delle Donne D, Di Lieto B, Esposito AM, Orazi M (2020) Geophysical precursors of the July-August 2019 paroxysmal eruptive phase and their implications for Stromboli volcano (Italy) monitoring. Sci Rep 10(1):10296

Giudicepietro F, Calvari S, D'Auria L et al (2022) Changes in the eruptive style of Stromboli volcano before the 2019 paroxysmal phase discovered through SOM clustering of seismo-acoustic features compared with camera images and GBInSAR data. Remote Sensing 14(5):1287

Giudicepietro F, Calvari S, De Cesare W et al (2023) Seismic and thermal precursors of crater collapses and overflows at Stromboli volcano. Sci Rep 13(1):11115

Hazlett RW, Buesch D, Anderson JL, Elan R, Scandone R (1991) Geology, failure conditions, and implications of seismogenic avalanches of the 1944 eruption at Vesuvius. Italy J Volcanol Geotherm Res 47(3–4):249–264

Heap MJ, Villeneuve M, Albino F et al (2020) Towards more realistic values of elastic moduli for volcano modelling. J Volcanol Geother Res 390:106684

Hoek E, Brown ET (2019) The Hoek-Brown failure criterion and GSI–2018 edition. J Rock Mech Geotech Eng 11(3):445–463

Hoek E, Carranza-Torres C (2002) Corkum B (2002) Hoek-Brown failure criterion-2002 edition. Proceedings of NARMS-Tac 1(1):267–273

Hoek E (2007) Practical rock engineering. 2007. Online. ed. Rocscience. https://www.rocscience.com/assets/resources/learning/hoek/Practical-Rock-Engineering-Full-Text.pdf . Accessed 14 March 2024.

Imbò G (1949) L'attività eruttiva vesuviana e relative osservazioni nel corso dell'intervallo eruttivo 1906–1944 ed in particolare del parossismo del marzo 1944. Annali dell'Osservatorio Vesuviano, V Serie, vol. unico, 1949. Published on 30 June 1951

James MR, Robson S (2012) Straightforward reconstruction of 3D surfaces and topography with a camera: accuracy and geoscience application. J Geophys Res Earth Surface 117(F3).

Kelfoun K, Samaniego P, Palacios P, Barba D (2009) Testing the suitability of frictional behaviour for pyroclastic flow simulation by comparison with a well-constrained eruption at Tungurahua volcano (Ecuador). Bull Volcanol 71:1057–1075

Kokelaar P, Romagnoli C (1995) Sector collapse, sedimentation and clast population evolution at an active island-arc volcano: Stromboli, Italy. Bull Volcanol 57:240–262

Krischer L et al (2015) Obspy: a bridge for seismology into the scientific Python ecosystem. Comput Sci Discov 8:014003. https://doi.org/10.1088/1749-4699/8/1/014003

Laiolo M, Delle Donne D, Coppola D, Bitetto M, Cigolini C, Della Schiava M, Innocenti L, Lacanna G, La Monica FP, Massimetti F, Pistolesi M (2022) Shallow magma dynamics at open-vent volcanoes tracked by coupled thermal and SO2 observations. Earth Planet Sci Lett 594:117726

Lerner GA, Jenkins SF, Charbonnier SJ, Komorowski JC, Baxter PJ (2022) The hazards of unconfined pyroclastic density currents: a new synthesis and classification according to their deposits, dynamics, and thermal and impact characteristics. J Volcanol Geotherm Res 421:107429

Lube G, Cronin SJ, Platz T, Freundt A, Procter JN, Henderson C, Sheridan MF (2007) Flow and deposition of pyroclastic granular flows: a type example from the 1975 Ngauruhoe eruption. New Zealand J Volcanol Geotherm Res 161(3):165–186

Marchetti E, Genco R, Ripepe M (2009) Ground deformation and seismicity related to the propagation and drainage of the dyke feeding system during the 2007 effusive eruption at Stromboli volcano (Italy). J Volcanol Geotherm Res 182(3–4):155–161

Martino M, Scifoni S, Marsella M, D'Aranno PJV, Napoleoni Q, Coltelli M (2015a) A multi-sensor approach for monitoring an active volcanic area: the 2011–2014 eruptive phase of Mount Etna. In: 2015 IEEE 15th International Conference on Environment and Electrical Engineering (EEEIC). IEEE, 2015. p. 1516–1521.

Martino M, Scifoni S, Napoleoni Q, D'Aranno PJV, Marsella M, Coltelli M (2015b) Integration of geotechnical modeling and remote sensing data to analyze the evolution of an active volcanic area: the case of the New South East Crater (Mount Etna). In Volcanic Rocks and Soils (pp. 179–180). CRC Press.

Marsella M, Baldi P, Coltelli M, Fabris M (2012) The morphological evolution of the Sciara del Fuoco since 1868: reconstructing the effusive activity at Stromboli volcano. Bull Volcanol 74:231–248

Massonnet M, Rossi M, Carmona C et al (1993) (1993) The displacement field of the Landers earthquake mapped by radar interferometry. Nature 364:138–142

Megies T, Beyreuther M, Barsch R, Krischer L, Wassermann J (2011) Obspy—What can it do for data centers and observatories? Ann Geophys-Italy 54:47–58. https://doi.org/10.4401/ag-4838

Monticelli T, Covelli N (1823) Storia de'fenomeni del Vesuvio, avvenuti negli anni 1821, 1822 e parte del 1823. Dai torchi del Gabinetto bibliografico e tipografico

Nairn IA, Self S (1978) Explosive eruptions and pyroclastic avalanches from Ngauruhoe in February 1975. J Volcanol Geotherm Res 3(1–2):39–60

Naismith A, Armijos MT, Escobar EAB, Chigna W, Watson IM (2020) Fireside tales: Understanding experiences of previous eruptions and factors influencing the decision to evacuate from activity of Volcán de Fuego. Volcanica 3(2):205–226

Natale A., Berardino P., Esposito C., Palmese G., Lanari R., Perna S. (2022) The new Italian airborne Multiband Interferometric and Polarimetric SAR (MIPS) system: first flight test results. International Geoscience and Remote Sensing Symposium 2022-IGARSS 2022, 4506–4509.

Nolesini T, Di Traglia F, Del Ventisette C, Moretti S, Casagli N (2013) Deformations and slope instability on Stromboli volcano: integration of GBInSAR data and analog modeling. Geomorphology 180:242–254

Norini G, De Beni E, Andronico D, Polacci M, Burton M, Zucca F (2009) The 16 November 2006 flank collapse of the south-east

crater at Mount Etna, Italy: Study of the deposit and hazard assessment. J Geophys Res: Solid Earth 114(B2)
Patrick MR, Harris AJ, Ripepe M, Dehn J, Rothery DA, Calvari S (2007) Strombolian explosive styles and source conditions: insights from thermal (FLIR) video. Bull Volcanol 69:769–784
Perna S, Esposito C, Amaral T et al (2016) The InSAeS4 Airborne X-Band Interferometric SAR System: a first assessment on its imaging and topographic mapping capabilities. Remote Sensing 8(1):40
Petronis MS, Delcamp A, Van Wyk De Vries B (2013) Magma emplacement into the Lemptégy scoria cone (Chaîne Des Puys, France) explored with structural, anisotropy of magnetic susceptibility, and Paleomagnetic data. Bul Volcanol 75:1–22
Pioli L, Azzopardi BJ, Cashman KV (2009) Controls on the explosivity of scoria cone eruptions: magma segregation at conduit junctions. J Volcanol Geotherm Res 186(3–4):407–415
Pioli L, Rosi M, Calvari S, Spampinato L, Renzulli A, Di Roberto A (2008) The eruptive activity of 28 and 29 December 2002. In: "The Stromboli Volcano: an integrated study of the 2002–2003 Eruption", American Geophysical Union Monograph Series, Calvari S., Inguaggiato S., Puglisi G., Ripepe M. and Rosi M. (Editors), v. 182, 105–116, 101029/182GM10. ISBN 978–0–87590–447–0.
Pistolesi M, Bertagnini A, Di Roberto A, Ripepe M, Rosi M (2020) Tsunami and tephra deposits record interactions between past eruptive activity and landslides at Stromboli volcano. Italy Geology 48(5):436–440
Ripepe M, Gordeev E (1999) Gas bubble dynamics model for shallow volcanic tremor at Stromboli. J Geophys Res Solid Earth 104(B5):10639–10654
Ripepe M, Lacanna G, Pistolesi M, Silengo MC, Aiuppa A, Laiolo M, Massimetti F, Innocenti L, Della Schiava M, Bitetto M, La Monica FP (2021) Ground deformation reveals the scale-invariant conduit dynamics driving explosive basaltic eruptions. Nat Comm 12(1):1683
Risica G, Rosi M, Pistolesi M, Speranza F, Branney MJ (2022) Deposit-derived block-and-ash flows: the hazard posed by perched temporary tephra accumulations on volcanoes; 2018 Fuego Disaster, Guatemala. J Geophys Res Solid Earth 127(6):e2021JB023699.
Rivalta E, Pascal K, Phillips J, Bonaccorso A (2013) Explosive expansion of a slowly decompressed magma analogue: evidence for delayed bubble nucleation. Geochem Geophys Geosyst 14(8):3067–3084
Rizzoli P, Martone M, Gonzalez C et al (2017) Generation and performance assessment of the global TanDEM-X digital elevation model. ISPRS J Photogramm Remote Sens 132:119–139
Rodríguez E, Morris CS, Belz JE (2006) A global assessment of the SRTM performance. Photogramm Eng Remote Sens 72(3):249–260
Romagnoli C, Casalbore D, Chiocci FL, Bosman A (2009a) Offshore evidence of large-scale lateral collapses on the eastern flank of Stromboli, Italy, due to structurally-controlled, bilateral flank instability. Marine Geol 262(1–4):1–13
Romagnoli C, Kokelaar P, Casalbore D, Chiocci FL (2009b) Lateral collapses and active sedimentary processes on the northwestern flank of Stromboli volcano. Italy Marine Geol 265(3–4):101–119
Rosen PA, Hensley S, Joughin IR, Li FK, Madsen SN, Rodríguez E, Goldstein RM (2000) Synthetic aperture radar interferometry. Proc IEEE 8(3):333–382
Rosi M, Pistolesi M, Bertagnini A, Landi P, Pompilio M, Di Roberto A (2013) Stromboli volcano, Aeolian Islands (Italy): present eruptive activity and hazards. Geol Soc London Mem 37(1):473–490
Rosi M, Levi ST, Pistolesi M et al (2019) Geoarchaeological evidence of middle-age tsunamis at Stromboli and consequences for the tsunami hazard in the southern Tyrrhenian Sea. Sci Rep 9(1):677
Rust AC, Cashman KV (2011) Permeability controls on expansion and size distributions of pyroclasts. J Geophys Res Solid Earth116(B11).
Saccorotti G, Chouet B, Martini M, Scarpa R (1998) Bayesian statistics applied to the location of the source of explosions at Stromboli volcano. Italy B Seismol Soc Am 88(5):1099–1111
Salvatici T, Di Roberto A, Di Traglia F et al (2016) From hot rocks to glowing avalanches: numerical modelling of gravity-induced pyroclastic density currents and hazard maps at the Stromboli volcano (Italy). Geomorphology 273:93–106
Sato H, Fujii T, Nakada S (1992) Crumbling of dacite dome lava and generation of pyroclastic flows at Unzen volcano. Nature 360(6405):664–666
Scarani A, Zandonà A, Di Fiore F, Valdivia P, Putra R, Miyajima N, Bornhöft H, Vona A, Deubener J, Romano C, Di Genova D (2022) A chemical threshold controls nanocrystallization and degassing behaviour in basalt magmas. Comm Earth Env 3(1):284
Schmid M, Kueppers U, Civico R, Ricci T, Taddeucci J, Dingwell DB (2021) Characterising vent and crater shape changes at Stromboli: implications for risk areas. Volcanica 4(1):87–105
Spampinato L, Calvari S, Oppenheimer C, Lodato L (2008) Shallow magma transport for the 2002–03 Mt. Etna eruption inferred from thermal infrared surveys. J Volcanol Geother Res 177:301–312. https://doi.org/10.1016/j.jvolgeores.2008.05.013
Speranza F, Pompilio M, D'Ajello Caracciolo F, Sagnotti L (2008) Holocene eruptive history of the Stromboli volcano: constraints from paleomagnetic dating. J Geophys Res Solid Earth 113(B9).
Tibaldi A (2001) Multiple sector collapses at Stromboli volcano, Italy: how they work. Bull Volcanol 63:112–125
Tibaldi A, Corazzato C, Marani M, Gamberi F (2009) Subaerial-submarine evidence of structures feeding magma to Stromboli volcano, Italy, and relations with edifice flank failure and creep. Tectonophysics 469(1–4):112–136
Turchi A, Di Traglia F, Gentile R, Fornaciai A, Zetti I, Fanti R (2022) Relative seismic and tsunami risk assessment for Stromboli island (Italy). Int J Disaster Risk Reduct 76:103002
Valade S, Lacanna G, Coppola D et al (2016) Tracking dynamics of magma migration in open-conduit systems. Bull Volcanol 78:78. https://doi.org/10.1007/s00445-016-1072-x

Valdivia P, Zandonà A, Kurnosov A, Ballaran TB, Deubener J, Di Genova D (2023) Are volcanic melts less viscous than we thought? The case of Stromboli basalt. Contrib Mineral Petrol 178(7):45

Voloschina M, Métrich N, Bertagnini A, Marianelli P, Aiuppa A, Ripepe M, Pistolesi M (2023) Explosive eruptions at Stromboli volcano (Italy): a comprehensive geochemical view on magma sources and intensity range. Bull Volcanol 85(6):1–21

Vossen CE, Cimarelli C, Bennett AJ, Schmid M, Kueppers U, Ricci T, Taddeucci J (2022) The electrical signature of mafic explosive eruptions at Stromboli volcano. Italy Sci Rep 12(1):9049

Yamamoto T, Takada A, Ishizuka Y, Miyaji N, Tajima Y (2005) Basaltic pyroclastic flows of Fuji volcano, Japan: characteristics of the deposits and their origin. Bull Volcanol 67:622–633

Authors and Affiliations

Federico Di Traglia[1,2] · Paolo Berardino[2] · Lorenzo Borselli[3,4] · Pierfrancesco Calabria[1] · Sonia Calvari[5] · Daniele Casalbore[6,7] · Nicola Casagli[8,9] · Francesco Casu[2] · Francesco Latino Chiocci[6,7] · Riccardo Civico[10] · Walter De Cesare[1] · Claudio De Luca[2] · Matteo Del Soldato[8] · Antonietta Esposito[1] · Carmen Esposito[2] · Massimiliano Favalli[11] · Alessandro Fornaciai[11] · Flora Giudicepietro[1,2] · Teresa Gracchi[8,9] · Riccardo Lanari[2] · Giovanni Macedonio[1,2] · Fernando Monterroso[2] · Antonio Natale[2] · Teresa Nolesini[12] · Stefano Perna[2,13] · Tullio Ricci[10] · Claudia Romagnoli[7,14] · Guglielmo Rossi[12] · Carlo Tacconi Stefanelli[8]

✉ Federico Di Traglia
federico.ditraglia@ingv.it

[1] Istituto Nazionale Di Geofisica E Vulcanologia, Osservatorio Vesuviano, Via Diocleziano 328, 80134 Napoli, Italy

[2] Consiglio Nazionale Delle Ricerche, Istituto Per Il Rilevamento Elettromagnetico Dell'Ambiente (CNR-IREA), Via Diocleziano 328, 80134 Naples, Italy

[3] Facultad de Ingenieria, Instituto de Geologia, Universidad Autonoma de San Luis Potosì (UASLP), Av. Dr. Manuel Nava 5, 78290 San Luis Potosí, Mexico

[4] Istituto Di Ricerca Per La Protezione Idrogeologica (CNR-IRPI), Consiglio Nazionale Delle Ricerche, Via Madonna Alta 126, 06128 Perugia, Italy

[5] Istituto Nazionale Di Geofisica E Vulcanologia, Osservatorio Etneo, Piazza Roma 2, 95125 Catania, Italy

[6] Dipartimento Di Scienze Della Terra, Università Degli Studi Di Roma "La Sapienza", Piazzale Aldo Moro 5, 00182 Rome, Italy

[7] Consiglio Nazionale Delle Ricerche, Istituto Di Geologia Ambientale E Geoingegneria (CNR-IGAG), UO Sapienza, Piazzale Aldo Moro, 7, 00185 Rome, RM, Italy

[8] Dipartimento Di Scienze Della Terra, Università Degli Studi Di Firenze, Via La Pira 4, 50121 Florence, Italy

[9] National Institute of Oceanography and Applied Geophysics - OGS, Borgo Grotta Gigante 42/C, 34010 Sgonico, Italy

[10] Istituto Nazionale Di Geofisica E Vulcanologia, Sezione Roma 1, Via Di Vigna Murata 605, 00143 Rome, Italy

[11] Istituto Nazionale Di Geofisica E Vulcanologia, Sezione Di Pisa, Via Cesare Battisti, 53-56125 Pisa, 56125 Pisa, Italy

[12] Centro Per La Protezione Civile, Università Degli Studi Di Firenze, Piazza San Marco 4, 50121 Florence, Italy

[13] Dipartimento Di Ingegneria, Università Degli Studi Di Napoli Parthenope, Naples, Italy

[14] Dipartimento Scienze Biologiche, Geologiche E Ambientali, Università Degli Studi Di Bologna, P.Za Porta S. Donato 1, 40126 Bologna, Italy